Article

Neuron

Phase Separation-Mediated TARP/MAGUK Complex Condensation and AMPA Receptor Synaptic Transmission

Graphical Abstract

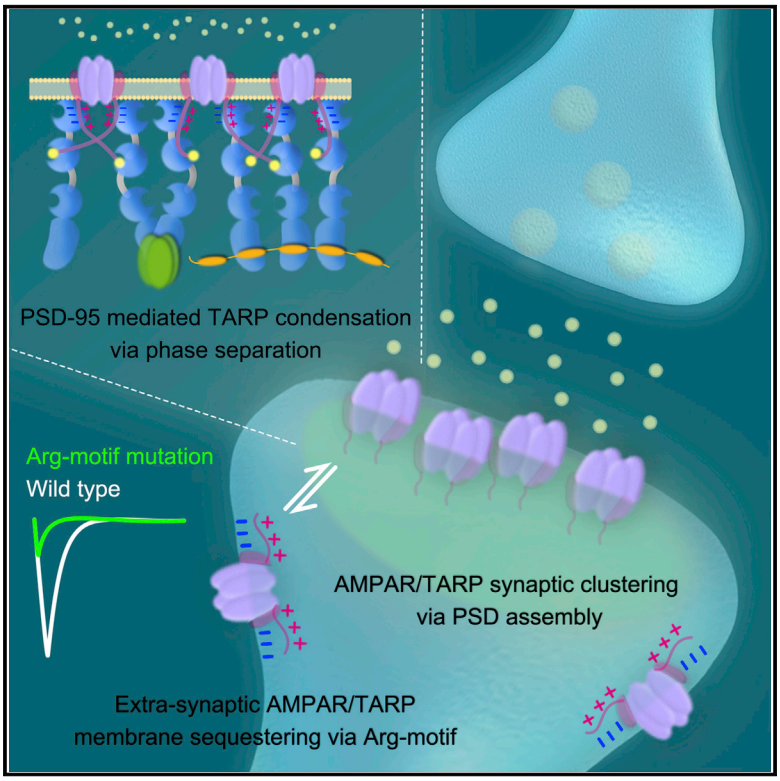

Highlights

- The entire tail of stargazin binds to PSD-95 with high affinity and specificity
- Stargazin/PSD-95 complex form condensed assembly via phase separation
- Other TARPs and MAGUKs interact with each other like stargazin/PSD-95 does
- Stargazin/PSD-95 phase separation is required for AMPAR synaptic transmission

Authors

Menglong Zeng, Javier Díaz-Alonso, Fei Ye, ..., Zeyang Ji, Roger A. Nicoll, Mingjie Zhang

Correspondence

mzhang@ust.hk

In Brief

Zeng et al. report that stargazin uses its entire C-terminal tail to bind to PSD-95 via a specific and multivalent interaction mode that governs the formation of condensed stargazin/PSD-95 assembly via liquid-liquid phase separation, a process critical for AMPAR synaptic targeting and transmission.

Zeng et al., 2019, Neuron *104*, 1–15
November 6, 2019
https://doi.org/10.1016/j.neuron.2019.08.001

CellPress

Please cite this article in press as: Zeng et al., Phase Separation-Mediated TARP/MAGUK Complex Condensation and AMPA Receptor Synaptic Transmission, Neuron (2019), https://doi.org/10.1016/j.neuron.2019.08.001

Neuron
Article

Phase Separation-Mediated TARP/MAGUK Complex Condensation and AMPA Receptor Synaptic Transmission

Menglong Zeng,[1,4] Javier Díaz-Alonso,[2,4] Fei Ye,[1] Xudong Chen,[1] Jia Xu,[1] Zeyang Ji,[1] Roger A. Nicoll,[2] and Mingjie Zhang[1,3,5,*]

[1]Division of Life Science, State Key Laboratory of Molecular Neuroscience, Hong Kong University of Science and Technology, Clear Water Bay, Kowloon, Hong Kong, China
[2]Department of Cellular and Molecular Pharmacology, University of California, San Francisco, San Francisco, CA 94143, USA
[3]Center of Systems Biology and Human Health, Hong Kong University of Science and Technology, Clear Water Bay, Kowloon, Hong Kong, China
[4]These authors contributed equally
[5]Lead Contact
*Correspondence: mzhang@ust.hk
https://doi.org/10.1016/j.neuron.2019.08.001

SUMMARY

Transmembrane AMPA receptor (AMPAR) regulatory proteins (TARPs) modulate AMPAR synaptic trafficking and transmission via disc-large (DLG) subfamily of membrane-associated guanylate kinases (MAGUKs). Despite extensive studies, the molecular mechanism governing specific TARP/MAGUK interaction remains elusive. Using stargazin and PSD-95 as the representatives, we discover that the entire tail of stargazin (Stg_CT) is required for binding to PSD-95. The PDZ binding motif (PBM) and an Arg-rich motif upstream of PBM conserved in TARPs bind to multiple sites on PSD-95, thus resulting in a highly specific and multivalent stargazin/PSD-95 complex. Stargazin in complex with PSD-95 or PSD-95-assembled postsynaptic complexes form highly concentrated and dynamic condensates via phase separation, reminiscent of stargazin/PSD-95-mediated AMPAR synaptic clustering and trapping. Importantly, charge neutralization mutations in TARP_CT Arg-rich motif weakened TARP's condensation with PSD-95 and impaired TARP-mediated AMPAR synaptic transmission in mice hippocampal neurons. The TARP_CT/PSD-95 interaction mode may have implications for understanding clustering of other synaptic transmembrane proteins.

INTRODUCTION

Targeting, clustering, and dynamic retention of AMPA receptors (AMPARs) to postsynaptic densities (PSDs) require a group of scaffold proteins known as the disc-large (DLG) subfamily of membrane-associated guanylate kinases (MAGUKs) (Chen et al., 2015; Elias et al., 2006; Elias and Nicoll, 2007; Feng and Zhang, 2009; Levy et al., 2015). Among them, PSD-95 is the prototypical member with the highest abundance in PSDs and plays critical roles in controlling AMPAR numbers and activity in excitatory synapses (Kim and Sheng, 2004; Sheng and Hoogenraad, 2007; Zhu et al., 2016). Overexpression of PSD-95 in hippocampal neurons enhances synaptic clustering and synaptic transmission of AMPARs without changing the overall AMPAR expression levels (Ehrlich and Malinow, 2004; El-Husseini et al., 2000b; Schnell et al., 2002). Simultaneous knockdown of PSD-95 and its two homologs, SAP102 and PSD-93, eliminates almost all AMPAR-mediated synaptic transmission in rat hippocampal organotypic cultures (Chen et al., 2015; Levy et al., 2015).

Interestingly, PSD-95 does not directly bind to AMPAR subunits. Instead, the association is mediated by a group of AMPAR auxiliary subunits termed transmembrane AMPAR regulatory proteins (TARPs) (Greger et al., 2017; Jackson and Nicoll, 2011). Members of the TARP family share a similar structure, with four transmembrane segments and a long C-terminal cytoplasmic tail (Figure 1A). TARPs directly couple to AMPARs through the transmembrane segments and the extracellular connecting loops (Twomey et al., 2016; Zhao et al., 2016) and bind to MAGUKs through their cytoplasmic tails (Bats et al., 2007; Chen et al., 2000; Dakoji et al., 2003; Schnell et al., 2002). TARPs are essential for many aspects of AMPAR functions, which include surface expression, synaptic targeting and clustering, and ligand gating properties (Greger et al., 2017; Jackson and Nicoll, 2011). The first TARP protein identified is stargazin (Stg), which is mutated in the stargazer mice with cerebellar ataxia and seizures (Letts et al., 1998). Stg mutation in the cerebellar granule cells results in lack of functional AMPAR currents, whereas the NMDA receptor (NMDAR)-mediated transmission is intact, underscoring the specific regulatory roles of Stg on AMPAR functions (Chen et al., 2000). Expression of a PDZ binding motif (PBM)-lacking mutant of Stg in granule cells from stargazer mice restored the membrane surface expression, but not the synaptic expression of AMPARs, indicating that the TARP PBM is essential for AMPAR synaptic targeting and/or retention of surface receptors (Chen et al., 2000). In living neurons, AMPARs undergo lateral diffusion on the plasma membrane and constantly

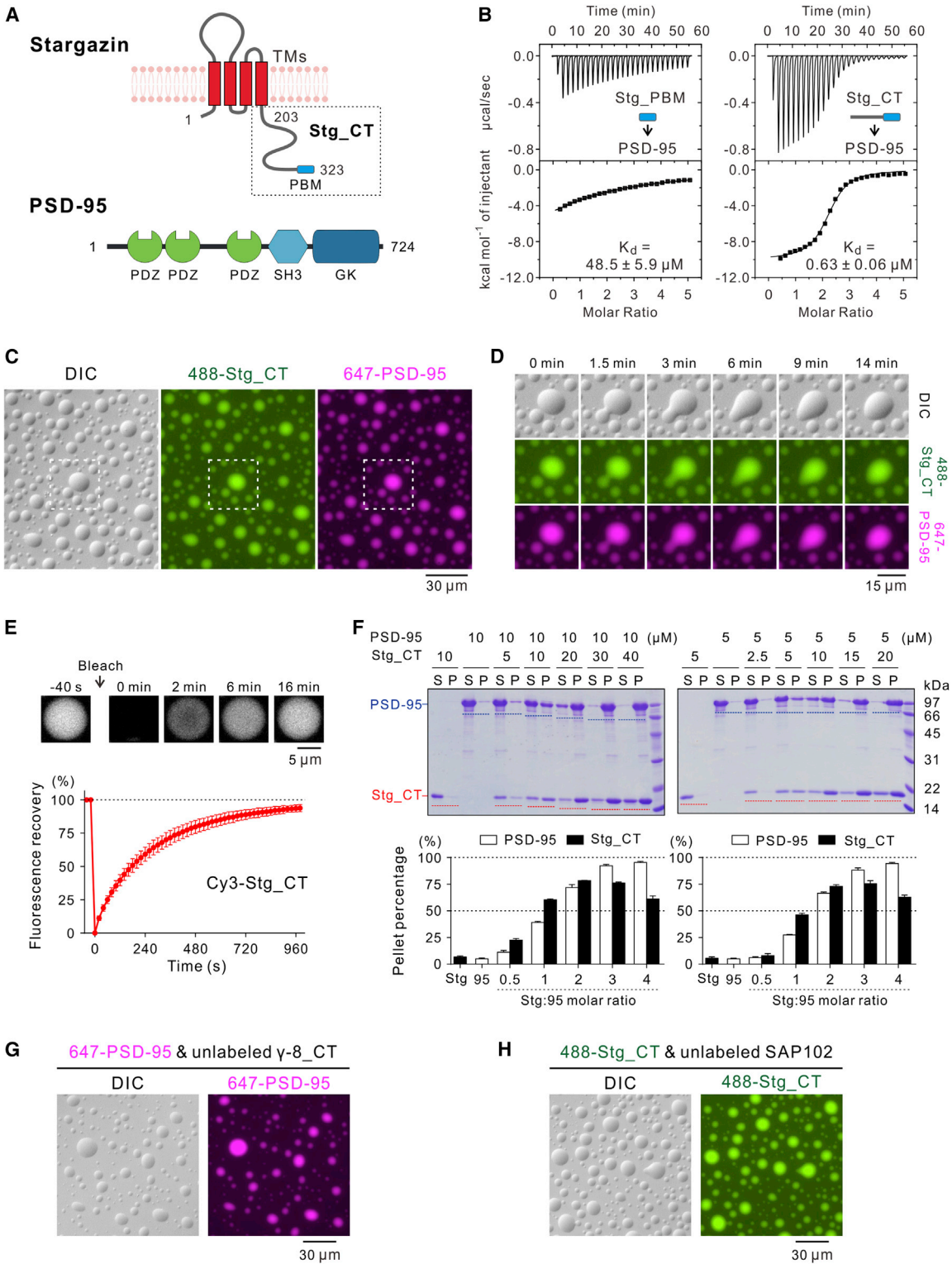

Figure 1. Specific Interaction between Stg_CT and PSD-95 Triggers Liquid-Liquid Phase Separation

(A) Schematic diagram showing the domain organization of Stg and PSD-95.

(B) ITC-based measurements comparing PSD-95 binding to Stg_PBM and Stg_CT. Stg_PBM or Stg_CT (250 µM) was titrated into PSD-95 (10 µM).

(legend continued on next page)

exchange between the extrasynaptic and synaptic sites. But the diffusion speed in synaptic sites is much slower than in extrasynaptic sites (Bats et al., 2007; Borgdorff and Choquet, 2002; Opazo et al., 2012). Mutation of TARP PBM increases AMPAR diffusion rates (Bats et al., 2007).

Although genetic and cellular data supporting TARPs/MAGUKs interaction with synaptic AMPARs are compelling, direct experimental data showing specific and direct binding between TARPs and MAGUK are surprisingly scarce. The majority of experimental data supporting the direct TARP/MAGUK binding are from TARP PBM deletion or mutation approach (Bats et al., 2007; Chen et al., 2000; Schnell et al., 2002; Sheng et al., 2018), which supports that TARP PBMs are necessary for binding to MAGUKs. The direct binding between TARP PBMs and PDZ domains of MAGUKs, although detectable by various methods (Dakoji et al., 2003; Hafner et al., 2015), is too weak (see Figure 1B) for the specific functional interaction between TARPs and MAGUKs observed *in vivo*, as PSDs contain numerous other PDZ domain proteins in addition to MAGUKs (Feng and Zhang, 2009; Kim and Sheng, 2004; Zhu et al., 2016).

In this study, we discover that the entire cytoplasmic tail of Stg (and other TARPs) is required for binding to PSD-95. The TARP PBM and an upstream Arg-rich motif together bind to PSD-95 PDZ12 with a previously unrecognized mode. Such multivalent Stg/PSD-95 binding triggers spontaneous condensation of the complex with other PSD proteins via liquid-liquid phase separation (LLPS) at physiological protein concentrations, which is reminiscent of ''trapping'' and clustering of the AMPAR/TARP complex at PSDs in living neurons. Such multivalent TARP/MAGUK interaction is essential for AMPAR synaptic transmission. The TARP/MAGUK interaction mode uncovered here elucidates the long sought after mechanism governing MAGUK-mediated AMPAR synaptic targeting and clustering via binding to TARPs.

RESULTS

The Entire C-Terminal Tail Is Required for the Specific and High-Affinity Binding of Stg to PSD-95

Previous studies of many PDZ/target interactions have suggested that a stretch of residues immediately preceding the canonical PBM (usually the last 4–6 residues) is often required for specific bindings of PDZ domain to their target proteins (Ye and Zhang, 2013; Zeng et al., 2016a, 2016b). To examine for such a possibility, we fused the last 20 residues of Stg (amino acids [aas] 304–323, denoted as Stg_PBM) to thioredoxin (Trx) and assayed the binding of Stg_PBM to the full-length PSD-95 (Figure 1A). Stg_PBM, with or without the Trx tag cleaved, binds to PSD-95 with a K_d of ~49 μM (Figure 1B; Table S1). It is noted that the binding of Stg_PBM to PSD-95 is much weaker than the majority of reported PSD-95 PDZ/target interactions, such as the NR2B tail/PSD-95 interaction (Long et al., 2003; Zeng et al., 2018).

The cytoplasmic tail of Stg contains 121 residues (Stg_CT; aas 203–323) and is highly conserved (Figures 1A and S1A). Unexpectedly, Stg_CT was found to bind to PSD-95 with a K_d of 0.63 μM, which is ~80-fold stronger than Stg_PBM does to PSD-95 (Figure 1B). The binding affinity between Stg_CT and PSD-95 is among the strongest of all PSD-95 PDZ12/target interactions reported.

Formation of the Stg_CT/PSD-95 Complex Triggers Molecular Condensation via Phase Separation

Mixing Stg_CT and PSD-95 led to formation of opalescent solutions. This reminded us of possible LLPS of the Stg_CT/PSD-95 complex similar to what we recently described for other PSD protein complexes (Zeng et al., 2016a, 2018). To verify this possibility, we labeled Stg_CT and PSD-95 with Alexa Fluor 488 and Alexa Fluor 647, respectively. When A647-PSD-95 (at 10 μM) and A488-Stg_CT (at 30 μM) were mixed at room temperature, we readily observed LLPS under light microcopy. Differential interference contrast (DIC) images revealed numerous spherical-shaped and micron-sized droplets. Fluorescence images showed that both Stg_CT and PSD-95 were highly enriched in the droplets (Figure 1C). Time-lapse imaging further showed that small droplets met and fused with each other (Figure 1D). Fluorescence recovery after photobleaching (FRAP) assay further revealed that Stg_CT in the droplets was constantly exchanging with molecules in the surrounding dilute solution (Figure 1E).

Sedimentation-based experiments were used to quantify the amount of proteins that formed the condensed phase (Zeng et al., 2016a, 2018). The LLPS efficiency of the Stg_CT/PSD-95 mixture was sensitive to the molar ratio of the two proteins. We first kept PSD-95 at 10 μM, and addition of increased amount of Stg_CT progressively promoted both proteins to be concentrated in the condensed phase (Figure 1F, left). With a saturating amount of Stg_CT at 30 μM or above, almost all PSD-95 was

(C) DIC and fluorescence images showing that the mixtures of 30 μM Alexa Fluor 488-labeled Stg_CT and 10 μM Alexa Fluor 647-labeled PSD-95 formed LLPS at room temperature and both components were highly co-enriched in micron-sized droplets. Only 1% of each protein was labeled by the indicated fluorophores, and this labeling ratio was used throughout this study unless otherwise specified. The dashed box is selected for zoom-in analysis in (D).

(D) Zoom-in and time-lapse images showing small droplets coalesced into larger ones (0–9 min) and the morphology of newly formed large droplet progressively relaxed to a spherical shape (9–14 min).

(E) FRAP assay showing the Stg_CT exchanging kinetics between the condensed droplets and surrounding aqueous solutions. Cy3-labeled Stg_CT (at 30 μM with only 0.5% of Stg_CT Cy3-labeled) was mixed with 10 μM unlabeled PSD-95. The curve represented the averaged signals from 10 droplets with a diameter ~9 μm, and the data were plotted as mean ± SD.

(F) Representative SDS-PAGE and quantification data of sedimentation experiments showing the distributions of Stg_CT and PSD-95 recovered from the aqueous phase or supernatant (S) and the condensed phase or pellet (P). Proteins were mixed at the indicated concentrations. Results were from 3 independent batches of sedimentation experiments and represented as mean ± SD.

(G and H) DIC and fluorescence images showing that the mixtures of (G) 30 μM unlabeled TARP γ-8_CT and 10 μM Alexa Fluor 647-labeled PSD-95 or (H) 30 μM Alexa Fluor 488-labeled Stg_CT and 10 μM unlabeled SAP102 formed LLPS at room temperature.

See also Figure S1.

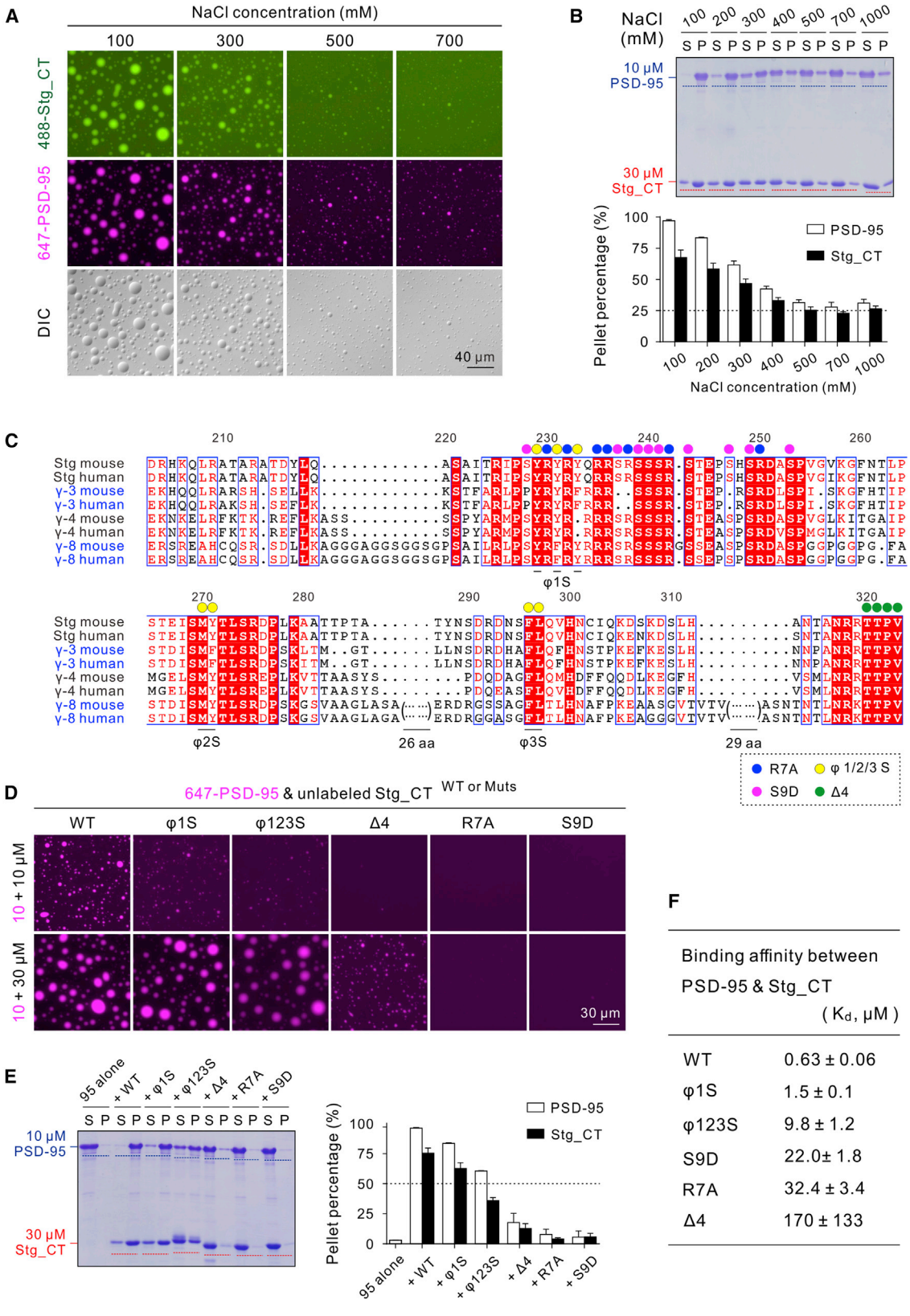

F

Binding affinity between PSD-95 & Stg_CT (K_d, μM)	
WT	0.63 ± 0.06
φ1S	1.5 ± 0.1
φ123S	9.8 ± 1.2
S9D	22.0± 1.8
R7A	32.4 ± 3.4
Δ4	170 ± 133

(legend on next page)

recovered in the pellet fraction. We next kept the Stg_CT and PSD-95 ratio unchanged but lowered the protein concentrations to half (Figure 1F, right). We observed a similar Stg_CT and PSD-95 ratio-dependent LLPS of the mixtures, except that the LLPS curve was right shifted (Figure 1F, right). The above imaging and sedimentation experiments demonstrated that the Stg_CT/PSD-95 complex can form self-assembled, highly condensed liquid droplets via LLPS at a few μM of the protein concentrations.

Phase-Separation-Mediated Condensation Is a General Property of TARP/MAGUK Complexes

Stg and other TARPs, including γ-3/4/8, have their discrete as well as overlapping expression patterns with respect to that of Stg. Nonetheless, their abilities to regulate AMPAR synaptic targeting and function are conserved (Jackson and Nicoll, 2011; Rouach et al., 2005; Tomita et al., 2003). The entire cytoplasmic tail of TARP γ-8 (aas 228–423; γ-8_CT) binds to PSD-95 with a K_d of ~9 μM (Figures S1A–S1C). We further showed that the γ-8_CT/PSD-95 complex, like the Stg_CT/PSD-95 complex, could also undergo LLPS (Figures 1G and S1B), except that γ-8_CT exhibited weaker LLPS capability with PSD-95 than Stg_CT did (Figure 1F, left, versus S1B), presumably due to its weaker binding to PSD-95. We also showed that Stg_CT interacted with SAP102 with a K_d of ~2 μM (Figure S1E). Additionally, SAP102 underwent LLPS with Stg_CT with a similar pattern as PSD-95 did (Figures 1H and 1F, left, versus S1D). The above experiments demonstrated that formation of highly concentrated molecular condensates is a general property of TARP/MAGUK complexes.

Molecular Determinants of Stg Governing Phase Separation of the Stg_CT/PSD-95 Complex

Stg_CT is intrinsically disordered and is enriched with Arg residues (Figure S2A). The LLPS of the Stg_CT/PSD-95 complex gradually decreased when NaCl concentrations in the assay buffer were increased from 100 mM to 500 mM (Figures 2A and 2B). Interestingly, the LLPS of the Stg_CT/PSD-95 complex was no longer sensitive to ionic strength when NaCl concentration was above 500 mM (Figures 2A and 2B), indicating that forces in addition to charge-charge interactions contribute to the phase separation of the complex.

We analyzed the tail sequences of all TARPs from different species and identified several conserved motifs (Figures 2C and S1A): (1) the last four residues as the canonical PBM are totally conserved in all TARPs; (2) a conserved Arg-rich motif (aas R230–R250 in mouse Stg) implicated to interact with lipid membranes (Hafner et al., 2015; Sumioka et al., 2010); (3) the Arg-rich motif is interspersed with a stretch of conserved Ser residues, some of which might be phosphorylation sites *in vivo* (Opazo et al., 2010; Park et al., 2016; Sumioka et al., 2010; Tomita et al., 2005); and (4) the tails of TARPs also contain three discrete aromatic residue-containing hydrophobic sites (referred to as φ1/2/3).

To test whether these conserved motifs are involved in Stg/PSD-95 LLPS, we constructed the following Stg_CT mutant proteins: (1) we deleted the last four residues (Δ4, shown with green circles) to test the role of the canonical PBM/PDZ interaction between Stg and PSD-95; (2) we substituted 7 highly conserved Args with Alas (R7A, blue circles) to probe the role of the charge-charge interactions; (3) we substituted 9 Sers within the Arg-rich motif with Asps to mimic their phosphorylation (S9D, magenta circles); and (4) we replaced hydrophobic residues in φ1 or in φ123 all together with Sers to assess the role of hydrophobic interactions (φ1S or φ123S, yellow circles; Figure 2C). All five mutant Stg_CT proteins were purified to high homogeneity (Figure S2B), and their LLPS abilities with PSD-95 were compared together with wild-type (WT) Stg_CT. The concentration of PSD-95 was fixed at 10 μM, and two different concentrations of Stg_CT (10 μM and 30 μM) were assayed. At the 10 μM plus 10 μM mixtures, the assay is highly sensitive to subtle changes of LLPS capacity of Stg_CT. Whereas at the 10 μM plus 30 μM mixtures, the assay is skewed toward the saturation condition for the WT proteins and thus is easier to detect large alterations to the LLPS capacity of Stg_CT (Figure 2D). When mixed at 10 μM with a 1:1 molar ratio, Stg_φ1S showed compromised LLPS, and Stg_φ123S had further reduced LLPS-forming capacity as indicated by fewer, smaller, and dimmer droplets. The Δ4, R7A, and S9D Stg mutants showed essentially no phase separation with PSD-95 under this more sensitive assay condition (Figure 2D, top row). At the Stg to PSD-95 molar ratio of 3:1, Stg_Δ4 exhibited obviously lower phase transition capacity with PSD-95 and the Stg_R7A and Stg_S9D mutants had essentially no detectable LLPS with PSD-95 (Figure 2D, bottom row). This result, together with the data from a sedimentation-based

Figure 2. Sequence Upstream of PBM Is Required for Stg_CT to Bind to PSD-95 and to Undergo LLPS

(A) DIC and fluorescence images showing high NaCl concentrations weakened but did not disrupt Stg_CT and PSD-95 LLPS. 30 μM Alexa Fluor 488-labeled Stg_CT were mixed with 10 μM Alexa-Fluor-647-labeled PSD-95 at indicated NaCl concentrations. Imaging settings in all panels were identical.

(B) Sedimentation assay showing progressively decreased LLPS of the Stg_CT and PSD-95 mixtures upon increasing NaCl concentrations. The LLPS levels reached a plateau of ~25% once NaCl concentration reached 500 mM or higher. Indicated concentrations of NaCl were added into protein mixtures containing 30 μM Stg_CT and 10 μM PSD-95.

(C) Sequence alignment showing conserved motifs identified in cytoplasmic tails of TARP family members. Mutated residues are denoted by colored circles as indicated. Two stretches of Gly- and Pro/Ala-rich sequences in TARP γ-8_CT are omitted but are shown in a more detailed alignment in Figure S1A.

(D) Fluorescence images showing a series of Stg_CT mutants with progressively weakened LLPS capability with PSD-95. 10 μM Alexa-Fluor-647-labeled PSD-95 was mixed with 10 μM or 30 μM unlabeled various forms of Stg_CT. Identical imaging settings were used for all groups.

(E) Sedimentation assay quantifying protein distributions in aqueous or condensed phases when mixed 10 μM PSD-95 with 30 μM Stg_CT proteins. The sedimentation results of apo-form Stg_CT proteins were in Figure S2B. The quantification results in (B) and (E) were from 3 independent batches of sedimentation experiments and represented as mean ± SD.

(F) ITC-measured binding affinities between PSD-95 and various forms of Stg_CT. The ITC raw data are listed in Figure S2C.

See also Figures S1 and S2.

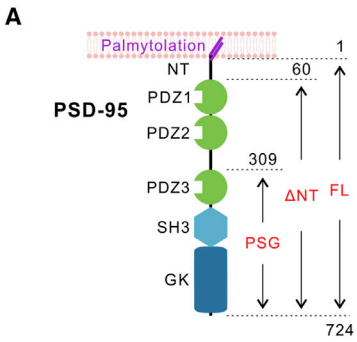

B

Binding affinity between PSD-95 & Stg_CT	(K_d, μM)
95_FL	0.63 ± 0.06
95_ΔNT	0.68 ± 0.03
95_PSG	5.3 ± 0.5

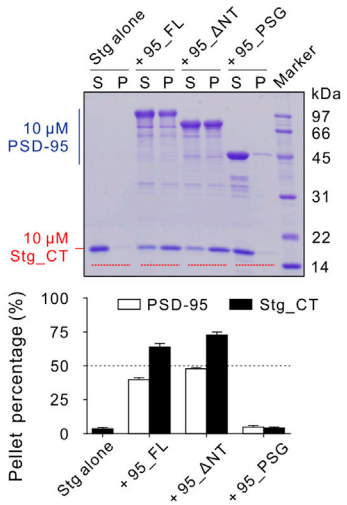

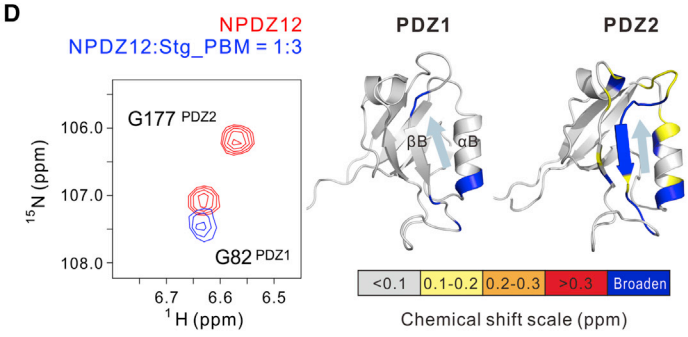

E

K_d (μM)	PDZ1	PDZ2
PBM	214 ± 91	40.2 ± 1.1
CT_WT	14.9 ± 0.8	19.7 ± 2.7
CT_R7A	58.5 ± 22.4	

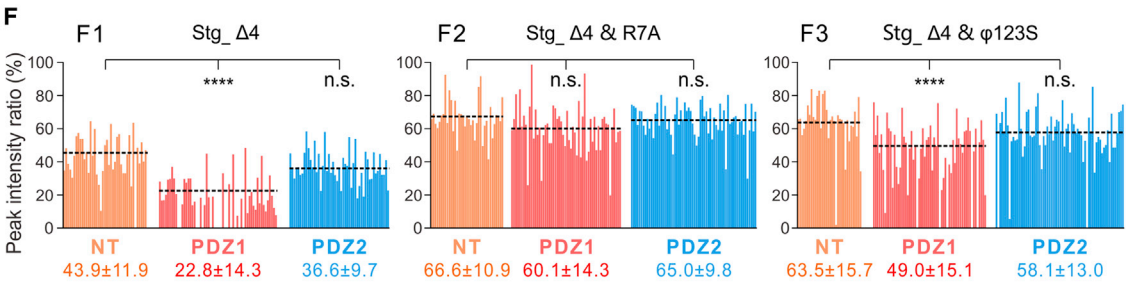

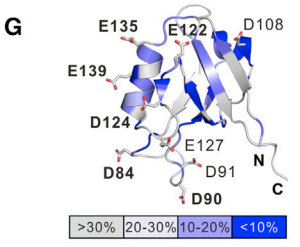

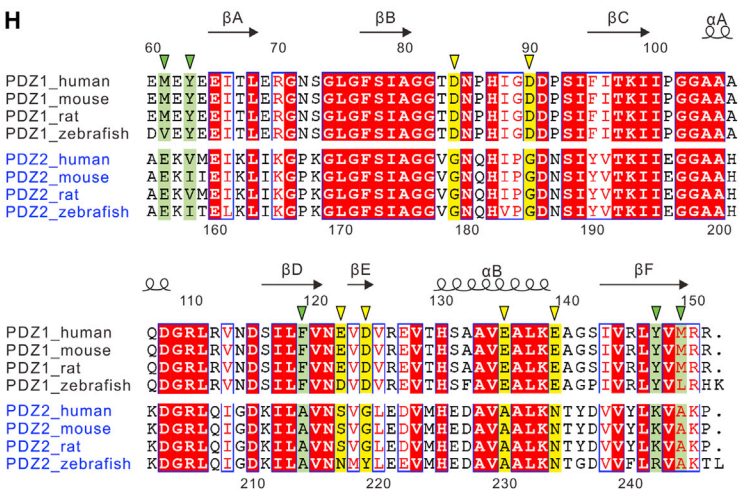

(legend on next page)

assay (Figure 2E), indicate that the LLPS capacities of the mutant Stg with PSD-95 progressively decreased in the order of φ1S, φ123S, Δ4, and R7A/S9D. The Stg_R7A and Stg_S9D were essentially not capable of forming condensates with PSD-95 in both assays.

Because Stg_CT alone is unstructured (Figure S2A) and did not undergo LLPS at concentrations up to 100 μM (Figure S3B), the weakened LLPS of the Stg mutants in their mixtures with PSD-95 must originate from their altered interactions with PSD-95. Indeed, Stg_φ1S, φ123S, S9D, R7A, and Δ4 all showed decreased binding to PSD-95 (Figure 2F). In particular, deletion of the PBM sequence had the largest impact on Stg_CT's binding to PSD-95. Both Stg_R7A and Stg_S9D showed large decreases in binding to PSD-95. The φ1S and φ123S mutants had milder impacts on PSD-95 binding.

PDZ1 and PDZ2 of PSD-95 Participate in Binding to Stg with Distinct Modes

How does PSD-95 bind to the elongated cytoplasmic tail of Stg_CT? We focused our structural analysis on the N-terminal half of PSD-95, including the unstructured N terminus (NT) (aas 1–59) and the PDZ12 tandem (aas 60–247) for several reasons: (1) EM studies revealed that the endogenous PSD-95 adopts a linear structure with its palmitoylated N terminus inserting perpendicularly into the plasma membranes (Chen et al., 2008; Figure 3A). Thus, the N-terminal half of PSD-95 is close to the synaptic membranes. (2) The C-terminal PDZ3-SH3-GK tandem (PSG) of PSD-95 is located in a deeper layer of PSDs and interacts with another set of proteins, including SynGAP and SAPAPs (Kim et al., 1997; Zeng et al., 2016a; Zhu et al., 2017). The binding between SynGAP C terminus and PSD-95 PSG (K_d value of ~0.2 μM; Zeng et al., 2016a) is several-dozen-fold stronger than that between Stg_CT and PSD-95 PSG (K_d value of ~5.3 μM; Figure 3B). (3) Overexpression of PSD-95 mutants lacking the first two PDZ domains is incapable of promoting AMPAR synaptic targeting (Schnell et al., 2002). (4) Our analysis also showed that the PDZ12 tandem of PSD-95 is critical for binding to Stg_CT and for forming phase-separated condensates. Specifically, removal of the unstructured N-terminal 59 residues of PSD-95 neither changed its binding to Stg_CT nor altered its LLPS with Stg_CT (Figures 3B and 3C). In contrast, PSD-95_PSG (aas 309–724) displayed a much weaker interaction and LLPS efficiency with Stg_CT (Figures 3B, 3C, and S3A). (5) The PDZ12 tandem of PSD-95, but neither of the PDZ domains alone, was capable of forming condensates with Stg_CT via LLPS (Figure S3B). In line with our biochemical data, overexpression of PSD-95 NPDZ12 potentiated AMPAR-mediated excitatory postsynaptic currents (AMPAR EPSCs) (Ehrlich and Malinow, 2004; Schnell et al., 2002).

To understand the molecular mechanism governing the interaction between PSD-95 PDZ12 and Stg_CT, we resorted to NMR spectroscopy. Formation of the condensed phase of the NPDZ12/Stg_CT complex prevented detailed NMR-based analysis due to dramatic line broadening. To overcome this challenge, we separated Stg_CT into two parts, Stg_PBM and the upstream sequence lacking the last 4 residues (Stg_Δ4). Neither Stg_PBM nor Stg_Δ4 underwent LLPS with NPDZ12 (data not shown). Titrating Stg_PBM into the ^{15}N-labeled NPDZ12 showed that PDZ2 exhibited much more obvious binding-induced chemical shift changes than PDZ1 did (Figures 3D and S4A), indicating that Stg_PBM preferably binds to PDZ2. Direct binding experiments showed that Stg_PBM binds to PDZ2 significantly stronger than to PDZ1 (Figures 3E and S3C). The NMR analysis further showed that Stg_PBM binds the canonical PBM binding pocket of PDZ2 (Figures 3D and S4A). Interestingly, Stg_CT bound to PDZ1 with a significantly stronger affinity than Stg_PBM did (Figures 3E and S3C), indicating that the sequence upstream of Stg_PBM could bind to PDZ1. In contrast, the difference of Stg_PBM and Stg_CT in binding to PDZ2 is minor (Figures 3E and S3D), indicating that PSD-95 PDZ2 specifically binds to the canonical PBM of Stg_CT.

We further used NMR spectroscopy to investigate the unexpected binding of Stg_Δ4 to PSD-95 PDZ12. We titrated unlabeled Stg_Δ4 into ^{15}N-labeled NPDZ12 and analyzed the binding-induced peak intensity changes of NT, PDZ1, and PDZ2 separately. Addition of Stg_Δ4 to NPDZ12 induced significant

Figure 3. The PDZ12 Tandem of PSD-95 Binds to the Entire Stg_CT with an Unexpected Mode

(A) Schematic diagram showing the perpendicular orientation of PSD-95 with respect to the PSD plasma membranes. The domain organization and boundary of PSD-95 fragments used in this study are indicated.

(B) Table listing the ITC-measured binding affinities between WT or truncated PSD-95 and Stg_CT. The affinities were measured by titrating 250 μM Stg_CT into 10 μM PSD-95_WT or ΔNT or 25 μM PSD-95_PSG.

(C) Sedimentation assay showing phase separation between 10 μM Stg_CT and 10 μM WT or truncated PSD-95. The quantification results were from 3 independent batches of sedimentations experiments and represented as mean ± SD. The sedimentation results of PSD-95 proteins alone are in Figure S3A.

(D) A selected region of ^{1}H,^{15}N HSQC spectra of PSD-95 NPDZ12 with or without three molar ratios of the Stg_PBM peptide (left, full spectra are shown in Figure S4A). Mapping of the backbone amide chemical shift changes of PDZ12 induced by Stg_PBM binding (right). The result was derived by comparing the ^{1}H,^{15}N HSQC spectra of apo form PDZ12 to those PDZ12 titrated with Stg_PBM.

(E) Table listing the ITC-measured binding affinities of Stg_PBM or Stg_CT to PSD-95 PDZ1 or PDZ2. The ITC raw data are listed in Figures S3C and S3D.

(F) Quantification of backbone amide peak broadening of PSD-95 NPDZ12 upon binding to Stg_CT_Δ4 mutants: Stg_CT_ Δ4 (F1); Stg_CT_ Δ4&R7A (F2); and Stg_CT_ Δ4&φ123S (F3). The average peak intensity of each domain is indicated by a dashed line. The peak intensity and error were represented as mean ± SD below each domain. Statistical significance was analyzed using one-way ANOVA with Bonferroni multiple comparison test. ****$p < 0.0001$; ns, not significant.

(G) Upper panel: mapping of the Stg_CT_Δ4 binding-induced backbone amide peak broadening of PDZ1 onto a clustered surface of the domain. Negative-charged residues located in this surface are drawn with the stick model. Lower panel: surface representation shows the electrostatic potential of PSD-95 PDZ1 contoured at ±3 kT/e.

(H) Sequence alignment analysis of PSD-95 PDZ1 and PDZ2, showing a high overall sequence identity between the two domains. Residues corresponding to the negative-charged residues that are uniquely conserved in PDZ1 are indicated using yellow triangles above the alignment. Hydrophobic residues that specifically conserved in PDZ1 are highlighted using green triangles.

See also Figures S3 and S4.

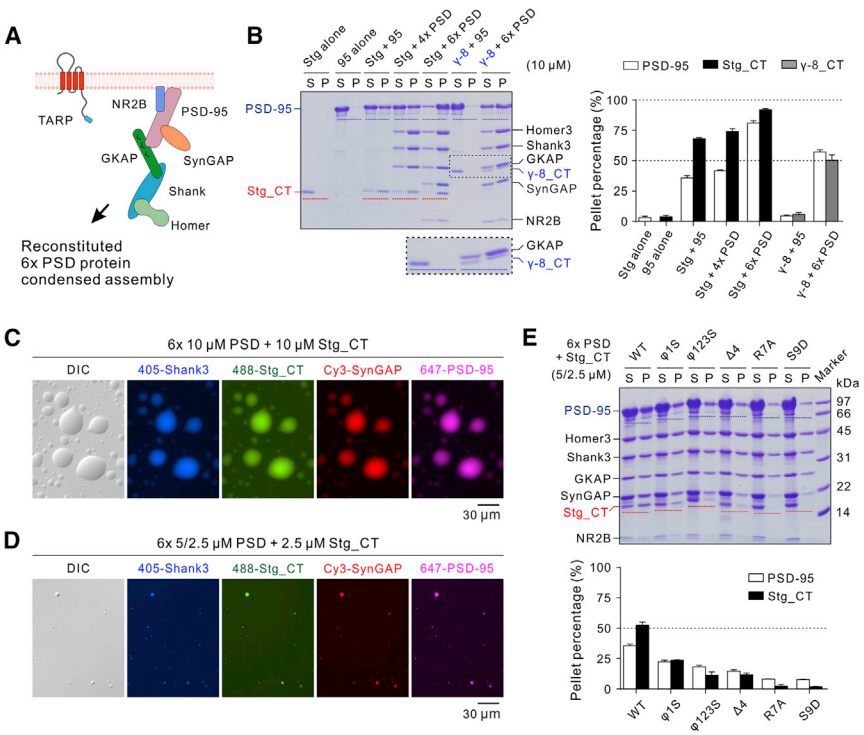

Figure 4. TARP_CT Incorporating into the Reconstituted 6× PSD Complexes through LLPS

(A) Schematic diagram showing the protein-interacting network of the reconstituted 6× PSD (Zeng et al., 2018).

(B) Sedimentation experiments showing the protein distributions of different PSD components in aqueous or condensed phases. 10 μM Stg_CT or TARP γ-8_CT were mixed with PSD-95 alone or 4× PSD (including PSD-95, GKAP, Shank3, and Homer3) or 6× PSD (including PSD-95, GKAP, Shank3, Homer3, SynGAP, and NR2B tail) with each component at 10 μM (except for NR2B at 20 μM; Zeng et al., 2018). Zoom-in of the dashed box shows the TARP γ-8_CT distribution. Quantifications of the TARPs and PSD-95 distributions are shown at right.

(C) DIC and fluorescence images showing the mixtures of 10 μM "Stg + 6× PSD" formed LLPS at room temperature. Stg_CT, PSD-95, Shank3, and SynGAP were labeled by different fluorophores as indicated and were highly co-concentrated in LLPS-mediated droplets. Homer3 and NR2B tail were not labeled and thus invisible. Each component was at 10 μM (except for NR2B at 20 μM).

(D) DIC and fluorescence images showing the mixtures of Stg + 6× PSD underwent LLPS at physiological protein concentrations and molar ratios. Proteins were labeled as illustrated in (C) above. 5 μM PSD-95 and SynGAP were mixed with GKAP, Shank3, Homer3, Stg_CT, and NR2B tail each at 2.5 μM.

(E) Sedimentation assay showing the LLPS levels of Stg_CT (WT and mutants) when mixed with 6× PSD at protein concentrations as illustrated in (D). The results in (B) and (E) were from 3 independent batches of sedimentation experiments and represented as mean ± SD.

peak broadening to PDZ1, but not obvious to NT and PDZ2 (Figure 3F1), indicating that PDZ1 is directly involved in binding to Stg_Δ4. We further introduced R7A or φ123S mutations to Stg_Δ4. Satisfyingly, the binding-induced peak broadening of PDZ1 was nearly completely disappeared for the Stg_Δ4&R7A mutant (Figure 3F2), supporting that the Arg-rich motif of Stg_CT is directly involved in binding to PSD-95 PDZ1. The peak broadening of PDZ1 was also less profound when Stg_Δ4&φ123S was titrated into NPDZ12 (Figure 3F3), indicating that the hydrophobic motifs of Stg_CT are also involved in binding to PSD-95 PDZ1. Isothermal titration calorimetry (ITC)-based binding assay showed the Stg_CT_R7A mutation displayed weaker binding to PDZ1 (Figures 3E and S3C3), further supporting the role of Stg Arg-rich motif in binding to PSD-95 PDZ1.

We mapped the residues in PDZ1 undergoing dramatic intensity decrease upon Stg_Δ4 binding to the PDZ1 structure and found that these residues are clustered on a surface opposite to its PBM binding pocket (Figures 3G and S4B). Notably, this surface is highly negatively charged (Figure 3G), fitting for binding to the Arg-rich motif in Stg_CT. Additionally, several hydrophobic residues are found in this negatively charged surface (Figure S4B), and these residues may be responsible for interacting with the Stg φ123 motifs. Further sequence analysis of PDZ1 and PDZ2 showed that, despite the overall sequence identity between PDZ1 and PDZ2 (~60.9% identity; Figure 3H), many of the negatively charged residues and exposed hydrophobic residues in PDZ1 surface are conserved in and unique to PDZ1 (Figure 3H, highlighted with triangles), explaining the specific interaction between Stg_Δ4 and PSD-95 PDZ1. Neutralization of six negatively charged residues on PDZ1 (indicated by yellow triangles in Figure 3H) by Asn weakened the PDZ1/Stg_CT binding by ~8-fold (Figure S3C4). Given the conserved sequence features of the TARP family members (Figure 2C), the binding between TARP γ-8 and PSD-95 likely also follows the same mechanism.

Stg_CT Undergoes LLPS with Reconstituted PSD Assembly at Physiological Concentrations

We recently showed that mixing four major PSD scaffold proteins (i.e., PSD-95/GKAP/Shank3/Homer3; 4× PSD) led to the formation of PSD-like condensates via LLPS. This PSD scaffold assembly can specifically enrich SynGAP and cluster NMDAR subunit NR2B tail. This six-component PSD assembly is termed as 6× PSD (Zeng et al., 2018). We next tested whether Stg_CT could also be condensed into this reconstituted PSD system via binding to PSD-95 (Figure 4A).

With each component concentration at 10 μM, Stg_CT underwent LLPS with both 4× PSD and 6× PSD assemblies, as indicated by the sedimentation and imaging assays (Figures 4B and 4C). In the "Stg + 6× PSD" mixture, there are four PSD-95 binding partners (i.e., Stg_CT, NR2B tail, SynGAP, and GKAP), which could either multimerize PSD-95 or contain multiple binding sites for PSD-95 (Zeng et al., 2018). Such expanded interaction network promoted PSD-95 to be more enriched in the condensed phase when compared to the Stg_CT and PSD-95 binary mixture (Figure 4B). The expanded PSD network also enhanced Stg_CT enrichment in the condensed phase. Similarly,

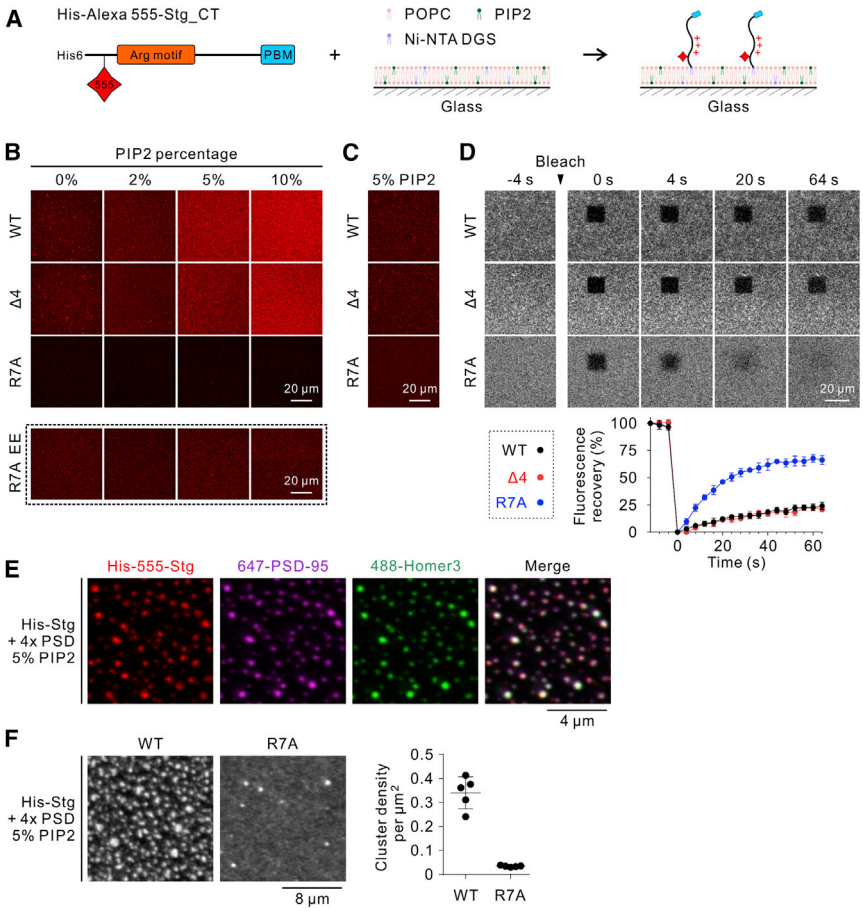

Figure 5. His-Stg_CT Undergoes Phase-Transition-Mediated Clustering with 4× PSD Scaffolds on Negatively Charged Lipid Bilayers

(A) Schematic diagram showing the design of His-Alexa Fluor 555-Stg_CT and its tethering to the supported negatively charged lipid bilayer.

(B) Confocal images showing the membrane bound levels of different His-Stg_CT variants with the presence of 0%–10% PIP2. Same concentration of His-Stg_CT (2 μM) was added to the system. In each variant, only 10% of His-Stg_CT was fluorescently labeled to avoid potential artifacts rendered by fluorescence probes. Same imaging parameters were applied for intensity comparison, except for the R7A EE group, in which elongated exposure time was applied to confirm R7A's membrane binding.

(C) Representative confocal images showing similar amount of His-Stg_CT were bound to the 5% PIP2- containing lipid bilayers. Initial protein concentrations were adjusted to WT/Δ4/R7A = 0.2/0.2/4 μM. Same initial protein concentrations were used in the experiments in (D)–(F).

(D) FRAP analysis comparing the mobility of different His-Stg_CT variants on lipid bilayers with the presence of 5% PIP2. The FRAP curves represented the averaged results from 5 bleached regions with a square-shaped size of 14 μm^2. Data were presented as mean ± SD.

(E) Confocal images showing His-Stg_CT clustering on negatively charged membrane upon addition of 4× PSD scaffolds (PSD-95, GKAP, Shank3, and Homer3, each at 2 μM; same concentrations were used in F). His-Alexa Fluor 555-Stg_CT was co-localized with Alexa Fluor 647-PSD-95 and Alexa Fluor 488-Homer3. GKAP and Shank3 were unlabeled and thus invisible.

(F) Confocal images showing R7A mutation profoundly diminished Stg_CT clustering upon addition of 4× PSD scaffolds. Each cluster was identified as an area larger than 0.05 μm^2 and with a mean fluorescent intensity at least three-folds higher than the mean fluorescent intensity before adding 4× PSD scaffolds. Data were presented as mean ± SD.

the 6× PSD system could dramatically enhance γ-8_CT in the PSD condensates (Figure 4B).

We next explored whether "Stg_CT + 6× PSD" LLPS could also occur at physiological protein concentrations and molar ratios. Each PSD on average contains approximately 300 copies of PSD-95/SynGAP: 150 copies of GKAP/Shank/Homer/TARP/PBM-containing tetrameric transmembrane proteins (Lowenthal et al., 2015; Sheng and Hoogenraad, 2007; Sugiyama et al., 2005). Assuming that, at the initial stage, these proteins are evenly distributed in an average-sized dendritic spine head with a volume ~0.1 μm^3, the starting concentrations of these proteins would be ~5 μM for PSD-95/SynGAP and ~2.5 μM for GKAP/Shank/Homer/TARP/NR2B tail. Accordingly, we mixed Stg_CT with the rest of six PSD components following the above-calculated concentrations. Indeed, the seven-component PSD mixture underwent LLPS, as evidenced by the imaging assay (Figure 4D). The sedimentation-based assay showed that ~50% of Stg_CT was recovered in the condensed phase in this seven-component mixture (Figure 4E). Importantly, we found that mutations on Stg_CT reduced the LLPS levels for both Stg_CT and PSD-95 (Figure 4E), with a pattern similar to that of the Stg_CT/PSD-95 binary system (Figures 2D and 2E). The amount of PSD-95 recovered in the pellet from the mixtures containing R7A or S9D Stg_CT was comparable to that from the mixture without addition of Stg_CT (data not shown).

Stg_CT Undergoes Phase-Transition-Mediated Clustering with 4× PSD on Negatively Charged Lipid Bilayers

We next asked whether TARPs can form LLPS-mediated clusters with PSD-95 and other PSD scaffolds on membranes (Zeng et al., 2018). In this assay, we first added an N-terminal 6× His tag to Stg_CT. We mutated the only Cys (Cys302) in Stg_CT to Ala and converted Ala212 outside the PSD-95 binding site to Cys for Alexa Fluor 555 labeling (Figure 5A). With this, we generated a system with Stg_CT on supported lipid bilayer, which mimics its *in vivo* conformation, where its N-terminal His tag binding to Ni-NTA DGS mimics the membrane tethering of Stg. We avoided large protein tags (e.g., a GFP tag) so the distances of various Stg_CT motifs (e.g., the Arg-rich motif) to the membrane surface are not altered.

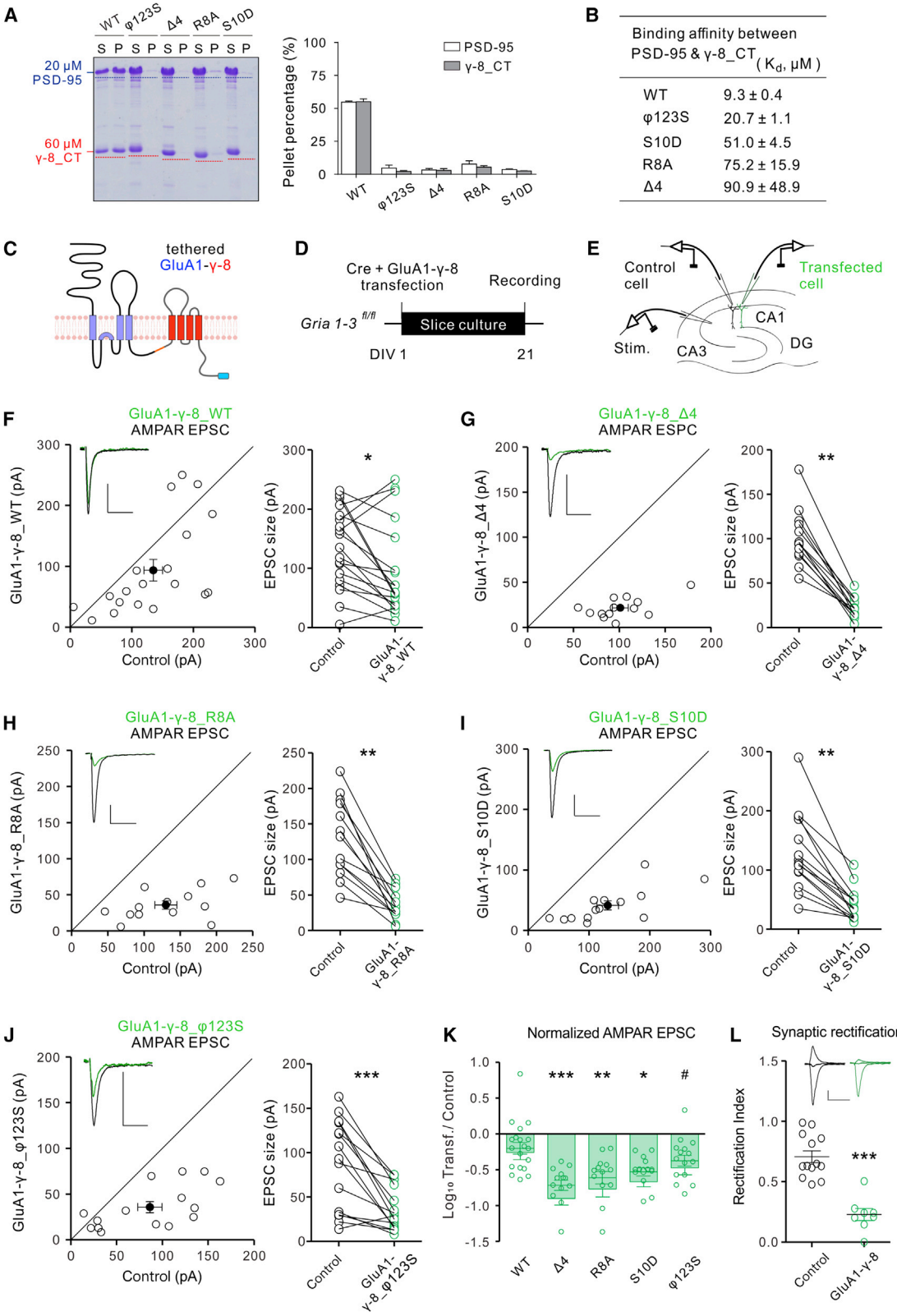

(legend on next page)

The basal lipid composition of our supported lipid bilayers consists of 97.9% 1-palmitoyl-2-oleoyl-glycero-3-phosphocholine (POPC), 2% Ni-1,2-dioleoyl-sn-glycero-3-[(N-(5-amino-1-carboxypentyl) iminodiacetic acid) succinyl] (NTA DGS), and 0.1% 1,2-dioleoyl-sn-glycero-3-phosphoethanolamine-N [methoxy (polyethylene glycol)-5000] (PEG5000) PE. His-Stg_WT could bind to the membranes with the basal lipid composition (Figure 5B; 0% phosphatidylinositol 4,5-bisphosphate [PIP2]). With increasing PIP2 concentrations, increasing amount of His-Stg_WT was bound to the membranes (Figure 5B). This observation is consistent with a previous report showing that Stg_CT binds to negatively charged lipid membranes (Sumioka et al., 2010). Lipid binding is mainly mediated by the Arg-rich motif, as His-Stg_Δ4 exhibited a similar membrane binding pattern as Stg_WT did but His-Stg_R7A displayed a much weaker membrane binding (Figure 5B).

We adjusted the initial input protein concentrations of different His-Stg_CT variants to achieve a comparable level of their initial membrane tethering (Figure 5C). We then performed FRAP experiments to compare the mobility of the three different His-Stg_CT variants on lipid bilayers containing 5% PIP2. R7A exhibited the fastest recovery rate after photobleaching, supporting that the Arg-rich motif is critical for Stg_CT to bind to membranes. Stg_CT WT and Δ4 showed much slower recovery rates, again in agreement with their similar membrane binding properties (Figure 5D).

We further assessed PSD complex-mediated clustering of Stg_CT on supported lipid bilayers. Upon addition of 4× PSD scaffolds (PSD-95, GKAP, Shank3, and Homer3, each at a concentration of 2 μM), we observed sub-micron-sized WT Stg_CT clusters formed on the membranes (Figure 5E). Confocal images confirmed these Stg_CT-enriched clusters were also co-enriched with PSD-95 and Homer3 (Figure 5E), suggesting clusters are promoted by the Stg/4× PSD scaffold-mediated LLPS.

Combining all of the above data together, we conclude that the Arg-rich motif plays a critical role in Stg_CT's binding to negatively charged membranes. But the membrane binding is not strong enough to sequester Stg_CT, because Stg_CT WT can still undergo LLPS upon interaction with PSD-95 and other PSD scaffolds on supported membrane bilayers containing 5% PIP2 (Figure 5E). Neutralizing the Arg-rich motif by R7A mutations weakened its interaction to the membranes and significantly increased its mobility on the PIP2-containing membranes (Figure 5D). The R7A mutation of His-Stg_CT also profoundly diminished the Stg/4× PSD LLPS capabilities on negatively charged lipid bilayers (Figure 5F), similar to the R7A behavior in solution (Figure 4E). With the above findings, we hypothesized that these TARP mutations, if introduced into living neurons, would also impair AMPAR/TARP clustering in PSDs.

TARP Mutants with Deficient LLPS Capabilities with PSD-95 Impair AMPAR EPSCs in Hippocampal Neurons

TARP γ-8 is the highest expressed TARP family member in the hippocampus (Rouach et al., 2005; Tomita et al., 2003). We first confirmed that the Arg-rich motif and three hydrophobic sites verified in Stg_CT are also important for the γ-8/PSD-95 interaction and LLPS (Figures 6A and 6B; see Figure S1 for detailed positions of the mutations). It is to be noticed that the pattern of PSD-95 binding reductions of the γ-8_CT mutants is very similar to that of the corresponding mutations of Stg_CT (Figure 6B versus 2F).

Next, we evaluated the impact of mutating these critical motifs in TARP γ-8 on AMPAR-mediated synaptic transmission. To unequivocally assess the functionality of mutant TARP γ-8, we biolistically transfected tethered GluA1-TARP_γ-8 (Figure 6C) together with Cre recombinase in organotypic hippocampal slices prepared from ~postnatal day 7 (P7) *Gria1-3*$^{fl/fl}$ mouse pups (Figure 6D). This experimental strategy allows the evaluation of the impact of TARP γ-8 mutations on AMPAR function by avoiding the confounding effects from the endogenous TARPs (Sheng et al., 2018). After allowing complete endogenous AMPAR removal in transfected cells for 3 weeks *in vitro* (Lu et al., 2009), we performed dual whole-cell recordings from CA1 pyramidal neurons, one transfected cell, and one neighboring control cell (Figure 6E). Replacement of endogenous AMPAR with GluA1 tethered to WT TARP γ-8 (GluA1-γ-8_WT) resulted in a substantial, although not complete, recovery of AMPAR EPSCs (control, 134.8 ± 15.3; transfected, 93.7 ± 17.7; p = 0.019; Figure 6F), whereas NMDAR synaptic currents were unaltered (control, 43.3 ± 7.2; transfected, 46.5 ± 9.8; p = 0.900; Figure S5B). Synaptic rectification was measured to confirm the complete removal of endogenous

Figure 6. AMPAR EPSCs upon Endogenous AMPAR Replacement with Tethered GluA1-γ-8

(A) Sedimentation experiments showing that, in contrast to WT TARP γ-8_CT, no LLPSs were observed when mixing 60 μM mutant forms TARP γ-8_CT and 20 μM PSD-95. The quantification results were from 3 independent batches of sedimentation experiments and represented as mean ± SD.

(B) Table listing the ITC-measured binding affinities between PSD-95 and different forms of TARP γ-8_CT. The raw data are shown in Figure S5A.

(C) Schematic diagram showing the topology of the tethered GluA1-γ-8.

(D) Scheme of the AMPAR replacement with tethered GluA1-γ-8 and timeline of the experiment.

(E) Scheme of simultaneous dual whole-cell recording in the hippocampus.

(F–J) Scatterplots of AMPAR EPSC for single pairs (open circles) of control and GluA1-γ-8_WT (F; n = 19 pairs), GluA1-γ-8_Δ4 (G; n = 13 pairs), GluA1-γ-8_R8A (H; n = 13 pairs), GluA1-γ-8_S10D (I; n = 14 pairs), or GluA1-γ-8_φ123S (J; n = 15 pairs). Filled circles represent mean ± SEM. Insets show sample current traces from control (black) and transfected (green) neurons. Scale bars: 50 pA, 50 ms.

(K) Summary plot comparing the $\log_{10}$ of the transfected or control neuron AMPAR EPSC ratio in all conditions tested.

(L) Endogenous AMPAR replacement with recombinant GluA1-γ-8 constructs resulted in rectified synaptic AMPAR currents (n = 13 control and 8 transfected cells).

Statistical significance was analyzed using the Wilcoxon signed-rank test in (F)–(J) and Mann-Whitney U test in (L). One-way ANOVA with Bonferroni multiple comparison test was used to compare relevant groups in (K). *p < 0.05, **p < 0.01, and ***p < 0.001 versus control condition. #p < 0.05 versus GluA1-γ-8_Δ4 condition.

See also Figures S5 and S6.

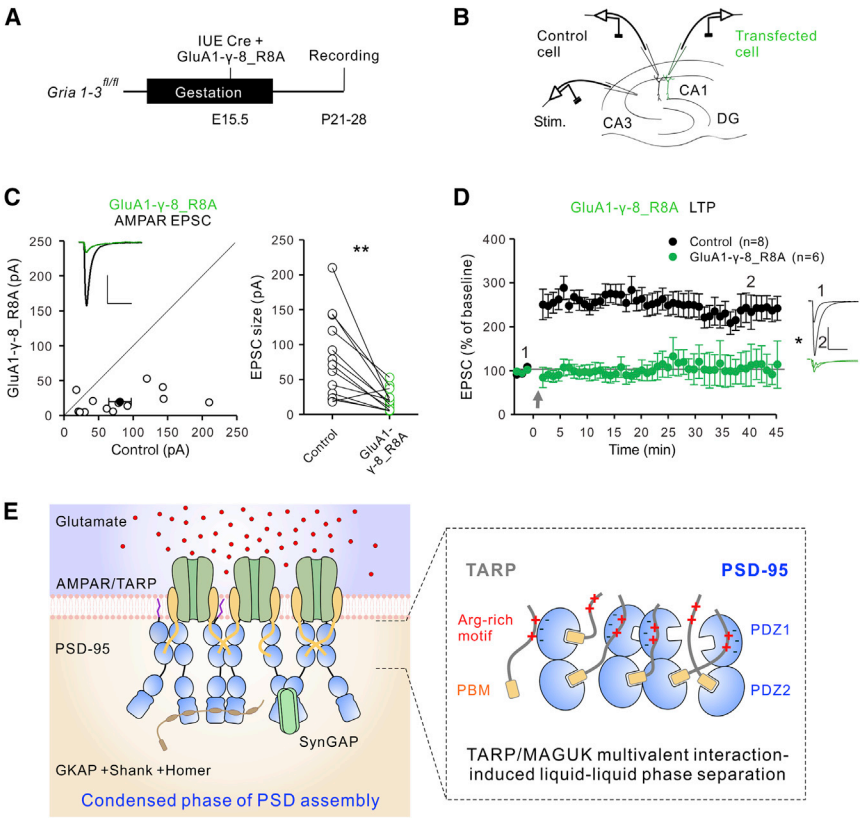

Figure 7. Long-Term Potentiation in GluA1-γ-8 R8A-Expressing CA1 Pyramidal Neurons and Working Model of AMPAR-TARP Synaptic Clustering

(A) Timeline of the experiment.

(B) Scheme of the AMPAR replacement strategy and dual whole-cell recordings from transfected (green) and control (black) CA1 pyramidal neurons.

(C) Scatterplot (left) and paired dot plot (right) of AMPAR EPSCs for single pairs (open circles) of control and Cre + GluA1-γ-8_R8A-expressing cells transfected by *in utero* electroporation (n = 13). Filled circle represents mean ± SEM. Inset shows sample current traces from control (black) and transfected (green) neurons.

(D) Plots showing mean ± SEM. AMPAR EPSC amplitude of control (black) and Cre + GluA1-γ-8_R8A-expressing CA1 pyramidal neurons normalized to the mean AMPAR EPSC amplitude before LTP induction (arrow). Insets show sample current traces before (1) and 40 min after (2) LTP induction from control (black) and transfected (green) neurons. LTP induction is indicated with a gray arrow. Scale bars: 50 pA, 50 ms. Statistical significance was analyzed using the Wilcoxon signed-rank test in (C). Mann-Whitney U test was used in (D). *p < 0.05; **p < 0.01.

(E) A model depicting AMPAR clustering at PSD via multivalent TARP/PSD-95 interaction-mediated condensate formation by LLPS.

GluA2 subunit, hence the homomeric nature of GluA1-TARP γ-8 AMPAR (control, 0.71 ± 0.05; transfected, 0.23 ± 0.05; p < 0.001; Figure 6L). Consistent with our previous observations (Sheng et al., 2018), replacement with GluA1-γ-8_Δ4 resulted in a dramatic reduction in the AMPAR EPSCs (control, 101.1 ± 8.7; transfected, 21.7 ± 3.2; p = 0.002; Figure 6G). This impairment was specific for AMPAR currents, because NMDAR EPSCs were unaltered (control, 32.8 ± 5.1; transfected, 28.5 ± 5.7; p = 0.349; Figure S5C). Replacement with GluA1-γ-8_R8A also resulted in a very pronounced decrease in AMPAR EPSCs (control, 130.4 ± 15.2; transfected, 36.0 ± 5.8; p = 0.002; Figure 6H). Again, NMDAR currents remained unchanged (control, 49.6 ± 8.2; transfected, 61.2 ± 11.9; p = 0.742; Figure S5D). AMPAR EPSCs were also significantly impaired in GluA1-γ-8_S10D (control, 130.8 ± 17.8; transfected, 41.4 ± 7.5; p = 0.001; Figure 6I). NMDAR EPSCs were not altered in this condition either (control, 35.2 ± 7.3; transfected, 30.0 ± 4.6; p = 0.401; Figure S5E). Finally, we tested the impact of the GluA1-γ-8_φ123S mutant. This mutant showed a milder though significant reduction in AMPAR EPSCs (control, 86.5 ± 13.2; transfected, 35.9 ± 6.2; p < 0.001; Figure 6J). NMDAR currents remained unaltered (control, 39.1 ± 6.6; transfected, 36.9 ± 4.6; p = 0.875; Figure S5F). The reduction of AMPAR EPSCs (Figure 6K) were nicely correlated with the γ-8_CT binding affinities with PSD-95 (Figure 6B), but the NMDAR EPSCs in all conditions were unaltered (Figure S5G), indicating that the multivalent TARP/MAGUK interaction is important for AMPAR synaptic targeting and synaptic transmission.

We further carried out paired recordings and puff-applied glutamate to cells. If surface delivery of the receptors is impaired, the AMPAR-mediated response should be diminished in the transfected cells. We examined GluA1-γ-8_WT, GluA1-γ-8_Δ4, GluA1-γ-8_R8A, GluA1-γ-8_S10D, and GluA1-γ-8_ φ123S. In none of these mutants did we find any effect on the response to applied glutamate (Figure S6). Thus, the synaptic defects arise from the inability of surface receptors to target to synapses.

Deficient TARP/PSD-95 LLPS Impairs Long-Term Potentiation (LTP) in Hippocampal Neurons

We next asked what role might the newly identified multivalent TARP/MAGUK interaction play in LTP. We previously showed that replacement of endogenous AMPAR with the GluA1-γ-8_Δ4 mutant construct abolishes LTP (Sheng et al., 2018). We now tested the role of the Arg-rich, motif-mediated TARP γ-8/PSD-95 interaction in LTP-mediated AMPAR trafficking using the GluA1-γ-8_R8A construct. To ensure that we are able to induce reliable LTP, we turned to acute slices, which we prepared from ~P23 *Gria1-3*$^{fl/fl}$ mice previously electroporated with a Cre-recombinase-expressing construct together with the GluA1-γ-8_R8A replacement construct at embryonic day 15.5 (E15.5) (Figure 7A). We then performed dual whole-cell recordings with one transfected and one control cell (Figure 7B). As expected from our slice culture experiments (Figures 6H and 6K), AMPAR replacement with GluA1-γ-8_R8A had a dramatic effect on the amplitude of evoked AMPAR currents (control, 81.2 ± 16.3; transfected, 19.9 ± 4.3, p = 0.001; Figure 7C).

We then compared LTP in GluA1-γ-8_R8A-expressing cells to neighboring control cells. Applying an LTP pairing protocol resulted in no LTP in transfected cells, and normal LTP was present in control cells (min 40: control, 2.4-fold change; transfected, 1.1-fold change, p = 0.029; Figure 7D).

DISCUSSION

Molecular Basis of the Specific Interaction between TARPs and DLG MAGUKs

We discover in this study that the entire C-terminal tail of Stg and γ-8 are engaged in binding to PSD-95. In this interaction, the canonical PBM of Stg binds to PDZ2 with a weak affinity and the upstream Arg-rich motif binds PDZ1 also with a weak affinity. This multivalent interaction between Stg_CT and PSD-95 results in a high overall binding affinity for the Stg_CT and PSD-95 complex. The binding mode elucidated in this study fits well with the geometric arrangements of both proteins beneath the PSD plasma membranes, in which the Arg-rich motif and PBM of Stg_CT bind to PDZ1 and PDZ2 of PSD-95, respectively (Figure 7E). The Arg-rich motif and PBM of Stg_CT are separated by a stretch of unstructured amino acid residues. As such, Stg_CT PBM can bind either to PDZ2 within the same PDZ12 tandem or PDZ2 from the neighboring PDZ12 tandem of PSD-95, resulting in a Stg/PSD-95 hetero-dimer or Stg/PSD-95 oligomers (Figure 7E). The formation of Stg/PSD-95 oligomers can lead to the formation of condensed Stg and PSD-95 complexes (or other TARP/MAGUK complexes) via LLPS. It is likely that the highly condensed PSD assembly in synapses can drive the condensation of Stg (and thus AMPAR), and Stg in return further promotes phase separation of the PSD assembly (Figure 7E). Our findings rationalize that the highly specific functional interactions between TARPs and MAGUKs are supported by their specific, strong, and direct interactions.

Several studies in the past have identified that the Arg-rich motif of TARPs is important for AMPAR synaptic targeting (Hafner et al., 2015; Sumioka et al., 2010). The key finding of these studies is that the Arg-rich motif of TARPs can directly interact with the negatively charged PSD membranes, resulting in membrane sequestration of the TARP cytoplasmic tails and consequent diminished PSD-95 binding. The authors proposed that phosphorylation of Ser residues in the Arg-rich motif can release Stg_CT from the plasma membrane and thereby promotes its binding to PSD-95 (Hafner et al., 2015; Opazo et al., 2010; Sumioka et al., 2010). Phosphomimetic mutations of Stg_CT were used to support their hypothesis. The present results do not directly address this mechanism. However, the fact that the phosphomimetic mutations greatly diminish the binding of TARP_CT to PSD-95 and that these mutations impair AMPARs EPSCs implies that the diminished binding to PSD-95 dominates.

The overall impact of the Stg_S9D mutation on PSD-95 binding found in the present study and in the previously published studies are apparently at odds (Hafner et al., 2015; Sumioka et al., 2010). In line with our study, Kessels et al. (2009) showed that expressing Stg_S9D or co-expressing Stg_S9D and GFP-GluA1 produced no potentiation to synaptic strength in hippocampal neurons. We demonstrated that the Stg_S9D and γ-8_S10D mutants have diminished binding to PSD-95 (Figures 2F and 6B), and γ-8_S10D also has impaired capacity in supporting AMPAR synaptic transmission (Figure 6I). In contrast, the Stg_S9D mutants in the previous biochemical studies were found to have no effect on PSD-95 binding (Sumioka et al., 2010) or increased Stg/PSD-95 interaction (Hafner et al., 2015) but did enhance AMPAR synaptic transmission (Sumioka et al., 2010; Tomita et al., 2005). Very different experimental approaches used between our study and the previous studies may account for the apparent discrepancies.

In living neurons, only two Ser residues of TARP γ-8_CT (Ser277 and Ser281) were substantially phosphorylated by CaMKII in synapses (Park et al., 2016). Interestingly, this selected Ser phosphorylation is enriched for TARP γ-8 in the PSD fraction, but not in the extrasynaptic fraction (Park et al., 2016), presumably due to the PSD enrichment of CaMKII. Therefore, it is possible that phosphorylation of a few Ser residues in the Arg-rich motif would promote TARP_CT dissociation from PSD membranes. However, such limited Ser phosphorylation may have a minor impact on the binding of the Arg-rich motif to PSD-95 PDZ1. Indeed, we found that the S277,281D mutant of TARP γ-8_CT had essentially the same PSD-95 binding affinity, and the mutation did not alter AMPAR EPSCs. However, the mutant had a weaker membrane binding (data not shown). Thus, the net outcome of Stg_CT phosphorylation would be to shift the balance toward enhanced TARP_CT/PSD-95 complex formation in PSD due to de-sequestration of the TARP_CT from the plasma membranes. Future work will be required to test such a model.

TARP/MAGUK LLPS and AMPAR Nanodomain Formation in Synapses

The distribution of AMPARs in synapses is not homogeneous. Recently, super-resolution light-microscopy-based studies revealed that neither AMPARs nor PSD-95 are uniformly distributed in synapses. Instead, they are co-enriched into condensed but dynamic nanodomains (MacGillavry et al., 2013; Nair et al., 2013). Interestingly, these AMPAR nanodomains seem to be aligned with presynaptic-vesicle-releasing machinery, forming *trans*-synaptic nanocolumn structures (Tang et al., 2016), a structural organization fitting for optimized synaptic transmission. We showed here that TARP_CT can undergo LLPS with major PSD scaffold proteins, like PSD-95, Shank3, and Homer3 at physiological concentrations (Figures 4 and 5). TARPs are highly enriched in condensed droplets with PSD proteins but also constantly exchanging with those in dilute solutions (Figure 1E). We also observed that small TARP/PSD-95-containing condensed droplets can coalesce into larger ones (Figure 1D), resembling the nanodomain reposition and fusion behaviors observed in living neurons (MacGillavry et al., 2013). Therefore, we propose that TARP/PSD scaffold-protein-mediated LLPS might be the underlying mechanisms of AMPAR nanodomains formation by spontaneously concentrating AMPAR/TARP complexes into dynamic condensates (Figure 7E). Notably, PSD-95 also interacts with synaptic adhesion molecules, like neuroligin (Irie et al., 1997), which can bridge with presynaptic adhesion molecules and thus contribute to the formation of *trans*-synaptic nanocolumns.

STAR★METHODS

Detailed methods are provided in the online version of this paper and include the following:

- KEY RESOURCES TABLE
- LEAD CONTACT AND MATERIALS AVAILABILITY
- EXPERIMENTAL MODEL AND SUBJECT DETAILS
  - Mice
  - Bacterial Strain
- METHOD DETAILS
  - Protein expression and purification
  - Protein fluorescence labeling
  - Phase transition sedimentation and imaging assay
  - Fluorescence recovery after photobleaching assay
  - Isothermal titration calorimetry assay
  - Lipid bilayer preparation and phase transition assay
  - NMR spectroscopy
  - Mouse genetics
  - Electrophysiology
  - *In vivo* AMPAR replacement
  - Acute slice electrophysiology and LTP induction
- QUANTIFICATION AND STATISTIC ANALYSIS
- DATA AND CODE AVAILABILITY

SUPPLEMENTAL INFORMATION

Supplemental Information can be found online at https://doi.org/10.1016/j.neuron.2019.08.001.

ACKNOWLEDGMENTS

This work was supported by grants from RGC of Hong Kong (AoE-M09-12 and C6004-17G); a 973 program grant from the Minister of Science and Technology of China (2014CB910204) to M. Zhang; a GRF grant from RGC of Hong Kong (16104518) to F.Y.; and RO1MH070957 and RO1MH117139 to R.N. J.D.-A. is supported by a NIH K99/R00 award (MH118425). M. Zhang is a Kerry Holdings Professor in Science and a Senior Fellow of IAS at HKUST.

AUTHOR CONTRIBUTIONS

M. Zeng, J.D.-A., F.Y., X.C., J.X., and Z.J. performed experiments; M. Zeng, J.D.-A., F.Y., X.C., J.X., R.A.N., and M. Zhang analyzed data; M. Zeng, R.A.N., and M. Zhang designed the research; M. Zeng, J.D.-A., F.Y., and M. Zhang drafted and all authors commented on the manuscript; and M. Zhang coordinated the research.

DECLARATION OF INTERESTS

The authors declare no competing interests.

Received: November 15, 2018
Revised: June 2, 2019
Accepted: July 29, 2019
Published: September 3, 2019

REFERENCES

Bats, C., Groc, L., and Choquet, D. (2007). The interaction between stargazin and PSD-95 regulates AMPA receptor surface trafficking. Neuron *53*, 719–734.

Borgdorff, A.J., and Choquet, D. (2002). Regulation of AMPA receptor lateral movements. Nature *417*, 649–653.

Chen, L., Chetkovich, D.M., Petralia, R.S., Sweeney, N.T., Kawasaki, Y., Wenthold, R.J., Bredt, D.S., and Nicoll, R.A. (2000). Stargazin regulates synaptic targeting of AMPA receptors by two distinct mechanisms. Nature *408*, 936–943.

Chen, X., Winters, C., Azzam, R., Li, X., Galbraith, J.A., Leapman, R.D., and Reese, T.S. (2008). Organization of the core structure of the postsynaptic density. Proc. Natl. Acad. Sci. USA *105*, 4453–4458.

Chen, X., Levy, J.M., Hou, A., Winters, C., Azzam, R., Sousa, A.A., Leapman, R.D., Nicoll, R.A., and Reese, T.S. (2015). PSD-95 family MAGUKs are essential for anchoring AMPA and NMDA receptor complexes at the postsynaptic density. Proc. Natl. Acad. Sci. USA *112*, E6983–E6992.

Dakoji, S., Tomita, S., Karimzadegan, S., Nicoll, R.A., and Bredt, D.S. (2003). Interaction of transmembrane AMPA receptor regulatory proteins with multiple membrane associated guanylate kinases. Neuropharmacology *45*, 849–856.

Delaglio, F., Grzesiek, S., Vuister, G.W., Zhu, G., Pfeifer, J., and Bax, A. (1995). NMRPipe: a multidimensional spectral processing system based on UNIX pipes. J. Biomol. NMR *6*, 277–293.

Díaz-Alonso, J., Sun, Y.J., Granger, A.J., Levy, J.M., Blankenship, S.M., and Nicoll, R.A. (2017). Subunit-specific role for the amino-terminal domain of AMPA receptors in synaptic targeting. Proc. Natl. Acad. Sci. USA *114*, 7136–7141.

Ehrlich, I., and Malinow, R. (2004). Postsynaptic density 95 controls AMPA receptor incorporation during long-term potentiation and experience-driven synaptic plasticity. J. Neurosci. *24*, 916–927.

El-Husseini, A.E., Schnell, E., Chetkovich, D.M., Nicoll, R.A., and Bredt, D.S. (2000b). PSD-95 involvement in maturation of excitatory synapses. Science *290*, 1364–1368.

Elias, G.M., and Nicoll, R.A. (2007). Synaptic trafficking of glutamate receptors by MAGUK scaffolding proteins. Trends Cell Biol. *17*, 343–352.

Elias, G.M., Funke, L., Stein, V., Grant, S.G., Bredt, D.S., and Nicoll, R.A. (2006). Synapse-specific and developmentally regulated targeting of AMPA receptors by a family of MAGUK scaffolding proteins. Neuron *52*, 307–320.

Feng, W., and Zhang, M. (2009). Organization and dynamics of PDZ-domain-related supramodules in the postsynaptic density. Nat. Rev. Neurosci. *10*, 87–99.

Greger, I.H., Watson, J.F., and Cull-Candy, S.G. (2017). Structural and functional architecture of AMPA-type glutamate receptors and their auxiliary proteins. Neuron *94*, 713–730.

Hafner, A.S., Penn, A.C., Grillo-Bosch, D., Retailleau, N., Poujol, C., Philippat, A., Coussen, F., Sainlos, M., Opazo, P., and Choquet, D. (2015). Lengthening of the stargazin cytoplasmic tail increases synaptic transmission by promoting interaction to deeper domains of PSD-95. Neuron *86*, 475–489.

Irie, M., Hata, Y., Takeuchi, M., Ichtchenko, K., Toyoda, A., Hirao, K., Takai, Y., Rosahl, T.W., and Südhof, T.C. (1997). Binding of neuroligins to PSD-95. Science *277*, 1511–1515.

Jackson, A.C., and Nicoll, R.A. (2011). The expanding social network of ionotropic glutamate receptors: TARPs and other transmembrane auxiliary subunits. Neuron *70*, 178–199.

Kessels, H.W., Kopec, C.D., Klein, M.E., and Malinow, R. (2009). Roles of stargazin and phosphorylation in the control of AMPA receptor subcellular distribution. Nat. Neurosci. *12*, 888–896.

Kim, E., and Sheng, M. (2004). PDZ domain proteins of synapses. Nat. Rev. Neurosci. *5*, 771–781.

Kim, E., Naisbitt, S., Hsueh, Y.P., Rao, A., Rothschild, A., Craig, A.M., and Sheng, M. (1997). GKAP, a novel synaptic protein that interacts with the guanylate kinase-like domain of the PSD-95/SAP90 family of channel clustering molecules. J. Cell Biol. *136*, 669–678.

Letts, V.A., Felix, R., Biddlecome, G.H., Arikkath, J., Mahaffey, C.L., Valenzuela, A., Bartlett, F.S., 2nd, Mori, Y., Campbell, K.P., and Frankel, W.N. (1998). The mouse stargazer gene encodes a neuronal Ca2+-channel gamma subunit. Nat. Genet. *19*, 340–347.

Levy, J.M., Chen, X., Reese, T.S., and Nicoll, R.A. (2015). Synaptic consolidation normalizes AMPAR quantal size following MAGUK loss. Neuron *87*, 534–548.

Long, J.F., Tochio, H., Wang, P., Fan, J.S., Sala, C., Niethammer, M., Sheng, M., and Zhang, M. (2003). Supramodular structure and synergistic target binding of the N-terminal tandem PDZ domains of PSD-95. J. Mol. Biol. *327*, 203–214.

Lowenthal, M.S., Markey, S.P., and Dosemeci, A. (2015). Quantitative mass spectrometry measurements reveal stoichiometry of principal postsynaptic density proteins. J. Proteome Res. *14*, 2528–2538.

Lu, W., Shi, Y., Jackson, A.C., Bjorgan, K., During, M.J., Sprengel, R., Seeburg, P.H., and Nicoll, R.A. (2009). Subunit composition of synaptic AMPA receptors revealed by a single-cell genetic approach. Neuron *62*, 254–268.

MacGillavry, H.D., Song, Y., Raghavachari, S., and Blanpied, T.A. (2013). Nanoscale scaffolding domains within the postsynaptic density concentrate synaptic AMPA receptors. Neuron *78*, 615–622.

Nair, D., Hosy, E., Petersen, J.D., Constals, A., Giannone, G., Choquet, D., and Sibarita, J.B. (2013). Super-resolution imaging reveals that AMPA receptors inside synapses are dynamically organized in nanodomains regulated by PSD95. J. Neurosci. *33*, 13204–13224.

Opazo, P., Labrecque, S., Tigaret, C.M., Frouin, A., Wiseman, P.W., De Koninck, P., and Choquet, D. (2010). CaMKII triggers the diffusional trapping of surface AMPARs through phosphorylation of stargazin. Neuron *67*, 239–252.

Opazo, P., Sainlos, M., and Choquet, D. (2012). Regulation of AMPA receptor surface diffusion by PSD-95 slots. Curr. Opin. Neurobiol. *22*, 453–460.

Park, J., Chávez, A.E., Mineur, Y.S., Morimoto-Tomita, M., Lutzu, S., Kim, K.S., Picciotto, M.R., Castillo, P.E., and Tomita, S. (2016). CaMKII phosphorylation of TARPγ-8 is a mediator of LTP and learning and memory. Neuron *92*, 75–83.

Rouach, N., Byrd, K., Petralia, R.S., Elias, G.M., Adesnik, H., Tomita, S., Karimzadegan, S., Kealey, C., Bredt, D.S., and Nicoll, R.A. (2005). TARP gamma-8 controls hippocampal AMPA receptor number, distribution and synaptic plasticity. Nat. Neurosci. *8*, 1525–1533.

Schnell, E., Sizemore, M., Karimzadegan, S., Chen, L., Bredt, D.S., and Nicoll, R.A. (2002). Direct interactions between PSD-95 and stargazin control synaptic AMPA receptor number. Proc. Natl. Acad. Sci. USA *99*, 13902–13907.

Sheng, M., and Hoogenraad, C.C. (2007). The postsynaptic architecture of excitatory synapses: a more quantitative view. Annu. Rev. Biochem. *76*, 823–847.

Sheng, N., Bemben, M.A., Díaz-Alonso, J., Tao, W., Shi, Y.S., and Nicoll, R.A. (2018). LTP requires postsynaptic PDZ-domain interactions with glutamate receptor/auxiliary protein complexes. Proc. Natl. Acad. Sci. USA *115*, 3948–3953.

Stoppini, L., Buchs, P.A., and Muller, D. (1991). A simple method for organotypic cultures of nervous tissue. J. Neurosci. Methods *37*, 173–182.

Sugiyama, Y., Kawabata, I., Sobue, K., and Okabe, S. (2005). Determination of absolute protein numbers in single synapses by a GFP-based calibration technique. Nat. Methods *2*, 677–684.

Sumioka, A., Yan, D., and Tomita, S. (2010). TARP phosphorylation regulates synaptic AMPA receptors through lipid bilayers. Neuron *66*, 755–767.

Tang, A.H., Chen, H., Li, T.P., Metzbower, S.R., MacGillavry, H.D., and Blanpied, T.A. (2016). A trans-synaptic nanocolumn aligns neurotransmitter release to receptors. Nature *536*, 210–214.

Tomita, S., Chen, L., Kawasaki, Y., Petralia, R.S., Wenthold, R.J., Nicoll, R.A., and Bredt, D.S. (2003). Functional studies and distribution define a family of transmembrane AMPA receptor regulatory proteins. J. Cell Biol. *161*, 805–816.

Tomita, S., Stein, V., Stocker, T.J., Nicoll, R.A., and Bredt, D.S. (2005). Bidirectional synaptic plasticity regulated by phosphorylation of stargazin-like TARPs. Neuron *45*, 269–277.

Twomey, E.C., Yelshanskaya, M.V., Grassucci, R.A., Frank, J., and Sobolevsky, A.I. (2016). Elucidation of AMPA receptor-stargazin complexes by cryo-electron microscopy. Science *353*, 83–86.

Wang, W., Weng, J., Zhang, X., Liu, M., and Zhang, M. (2009). Creating conformational entropy by increasing interdomain mobility in ligand binding regulation: a revisit to N-terminal tandem PDZ domains of PSD-95. J. Am. Chem. Soc. *131*, 787–796.

Ye, F., and Zhang, M. (2013). Structures and target recognition modes of PDZ domains: recurring themes and emerging pictures. Biochem. J. *455*, 1–14.

Zeng, M., Shang, Y., Araki, Y., Guo, T., Huganir, R.L., and Zhang, M. (2016a). Phase transition in postsynaptic densities underlies formation of synaptic complexes and synaptic plasticity. Cell *166*, 1163–1175.e12.

Zeng, M., Shang, Y., Guo, T., He, Q., Yung, W.H., Liu, K., and Zhang, M. (2016b). A binding site outside the canonical PDZ domain determines the specific interaction between Shank and SAPAP and their function. Proc. Natl. Acad. Sci. USA *113*, E3081–E3090.

Zeng, M., Chen, X., Guan, D., Xu, J., Wu, H., Tong, P., and Zhang, M. (2018). Reconstituted postsynaptic density as a molecular platform for understanding synapse formation and plasticity. Cell *174*, 1172–1187.e16.

Zhao, Y., Chen, S., Yoshioka, C., Baconguis, I., and Gouaux, E. (2016). Architecture of fully occupied GluA2 AMPA receptor-TARP complex elucidated by cryo-EM. Nature *536*, 108–111.

Zhu, J., Shang, Y., and Zhang, M. (2016). Mechanistic basis of MAGUK-organized complexes in synaptic development and signalling. Nat. Rev. Neurosci. *17*, 209–223.

Zhu, J., Zhou, Q., Shang, Y., Li, H., Peng, M., Ke, X., Weng, Z., Zhang, R., Huang, X., Li, S.S.C., et al. (2017). Synaptic targeting and function of SAPAPs mediated by phosphorylation-dependent binding to PSD-95 MAGUKs. Cell Rep. *21*, 3781–3793.

STAR★METHODS

KEY RESOURCES TABLE

REAGENT or RESOURCE	SOURCE	IDENTIFIER
Chemicals, Peptides, and Recombinant Proteins		
Recombinant protein: Stg_CT WT or mutants (φ1S, φ123S, S9D, R7A, Δ4) (203D-323V; NCBI, NP_031609; mutation sites are illustrated in Figure 2C)	This paper	N/A
Recombinant protein: His-Stg_CT WT or mutants (R7A and Δ4) (His6-203D-323V; NCBI, NP_031609; Both WT and mutants contain double-residue substitution (A212C + C302A) for Cys-labeling)	This paper	N/A
Recombinant protein: TRX-Stg_PBM (TRX-304Q-323V; NCBI, NP_031609)	This paper	N/A
Recombinant protein: TARP γ-8_CT WT or mutants (φ123S, S10D, R8A, Δ4) (228E-423V, lacking A341-A349 in our template; NCBI, NP_573453; mutation sites are illustrated in Figure S1A)	This paper	N/A
Recombinant protein: PSD-95 Full length (aa 1M-724L, UniProt: P78352-1)	Zeng et al., 2018	N/A
Recombinant protein: PSD-95 PDZ1 WT or mutant (ED6N) (aa 60E-151R UniProt: P78352-1, mutation sites are illustrated in Figure 3H)	This paper	N/A
Recombinant protein: PSD-95 PDZ2 (aa 155A-247S, UniProt: P78352-1)	This paper	N/A
Recombinant protein: PSD-95 PDZ12 (aa 60E-247S, UniProt: P78352-1)	This paper	N/A
Recombinant protein: PSD-95 NPDZ12 (aa 1M-247S, UniProt: P78352-1)	This paper	N/A
Recombinant protein: PSD-95 PSG (aa 309R-724L, UniProt: P78352-1)	Zeng et al., 2018	N/A
Recombinant protein: PSD-95 ΔNT (aa 60E-724L, UniProt: P78352-1)	This paper	N/A
Recombinant protein: SAP102 Full length (aa 1M-849L, NCBI, NP_113827)	This paper	N/A
Recombinant protein: GKAP (6x PSD component)	Zeng et al., 2018	N/A
Recombinant protein: Shank3 (6x PSD component)	Zeng et al., 2018	N/A
Recombinant protein: Homer3 (6x PSD component)	Zeng et al., 2018	N/A
Recombinant protein: SynGAP (6x PSD component)	Zeng et al., 2018	N/A
Recombinant protein: NR2B (6x PSD component)	Zeng et al., 2018	N/A
$^{15}NH_4Cl$	Cambridge Isotope	Cat#NLM-467-PK
iFluor 405 succinimidyl ester	AAT Bioquest	Cat#1021
Alexa Fluor 488 succinimidyl ester	ThermoFisher	Cat#A20000
Cy3 monosuccinimidyl ester	AAT Bioquest	Cat#271
Alexa Fluor 647 carboxylic acid, succinimidyl ester	Invitrogen	Cat#A20006
iFluor 555 maleimide	AAT Bioquest	Cat# 1063
POPC	Avanti	Cat#850457P
DGS-NTA(Ni)	Avanti	Cat#790404P
PEG5000 PE	Avanti	Cat#880230P

(*Continued on next page*)

Continued

REAGENT or RESOURCE	SOURCE	IDENTIFIER
PIP2	Echelon Biosciences	Cat#P-4516
D-APV	Cayman Chemical	Cat# 14539
Bicuculline	SIGMA-ALDRICH	Cat # 14340
2-Chloroadenosine	SIGMA-ALDRICH	Cat # C5134
Critical Commercial Assays		
Helios Gene Gun Kit	Bio-Rad	Cat# 1652411
Helios Cartridge Kit	Bio-Rad	Cat# 1652440
Experimental Models: Organisms/Strains		
Escherichia coli BL21 (DE3) cells	Invitrogen	Cat# C600003
Stellar Competent Cells	Takara Bio	Cat# 636763
C57BL6/N Gria1-3f/f mice	Lu et al., 2009	N/A
Recombinant DNA		
Plasmid for recombinant protein expression: Stg_CT WT or mutants (φ1S, φ123S, S9D, R7A, Δ4)	This paper	N/A
Plasmid for recombinant protein expression: His-Stg_CT WT or mutants (R7A and Δ4)	This paper	N/A
Plasmid for recombinant protein expression: TRX-Stg_PBM	This paper	N/A
Plasmid for recombinant protein expression: TARP γ-8_CT WT or mutants (φ123S, S10D, R8A, Δ4)	This paper	N/A
Plasmid for recombinant protein expression: PSD-95 Full length	Zeng et al., 2018	N/A
Plasmid for recombinant protein expression: PSD-95 PDZ1 WT or mutant (ED6N)	This paper	N/A
Plasmid for recombinant protein expression: PSD-95 PDZ2	This paper	N/A
Plasmid for recombinant protein expression: PSD-95 PDZ12	This paper	N/A
Plasmid for recombinant protein expression: PSD-95 NPDZ12	This paper	N/A
Plasmid for recombinant protein expression: PSD-95 PSG	Zeng et al., 2018	N/A
Plasmid for recombinant protein expression: PSD-95 ΔNT	This paper	N/A
Plasmid for recombinant protein expression: SAP102 Full length	This paper	N/A
Plasmid for recombinant protein expression: GKAP (6x PSD component)	Zeng et al., 2018	N/A
Plasmid for recombinant protein expression: Shank3 (6x PSD component)	Zeng et al., 2018	N/A
Plasmid for recombinant protein expression: Homer3 (6x PSD component)	Zeng et al., 2018	N/A
Plasmid for recombinant protein expression: SynGAP (6x PSD component)	Zeng et al., 2018	N/A
Plasmid for recombinant protein expression: NR2B (6x PSD component)	Zeng et al., 2018	N/A
Plasmid for recombinant protein expression: pCAGGS-GluA1-TARP γ-8_ WT or mutants (φ123S, S10D, R8A, Δ4)-IRES GFP	This paper	N/A

(*Continued on next page*)

Continued

REAGENT or RESOURCE	SOURCE	IDENTIFIER
Plasmid for recombinant protein expression: pFUGW-Cre:GFP	Díaz-Alonso et al., 2017	N/A
Software and Algorithms		
Origin7.0	OriginLab	https://www.originlab.com/
PyMOL	PyMOL	http://pymol.sourceforge.net/
ASTRA6	Wyatt	https://www.wyatt.com/products/software/astra.html
ImageJ	NIH	https://imagej.nih.gov/ij/
Prism	GraphPad	https://www.graphpad.com/scientific-software/prism/
NMRPipe	(Delaglio et al., 1995)	https://spin.niddk.nih.gov/bax/software/NMRPipe/
Sparky	T. D. Goddard and D. G. Kneller, SPARKY, University of California, San Francisco	https://www.cgl.ucsf.edu/home/sparky/
Igor Pro	Wavemetrics	https://www.wavemetrics.com/products/igorpro

LEAD CONTACT AND MATERIALS AVAILABILITY

Plasmids generated in this study do not appear to be generic and unique and thus are not deposited in public repositories. Further information and requests for resources and reagents should be directed to and will be fulfilled by the Lead Contact, Mingjie Zhang (mzhang@ust.hk).

EXPERIMENTAL MODEL AND SUBJECT DETAILS

Mice

Gria1–3$^{fl/fl}$ C57BL6/N mice used in this study were genotyped as previously described (Lu et al., 2009). Slice cultures were prepared from P6–P8 *Gria1–3*$^{fl/fl}$ mouse pups of either sexes. All mice were maintained under a 12:12 hour L/D schedule according to the UCSF IACUC guidelines. All protocols were approved by the IACUC at University of California, San Francisco, in full compliance with NIH guidelines for humane treatment of animals.

Bacterial Strain

Escherichia coli BL21 (DE3) cells used for protein expressions were from Invitrogen under the category # of C600003.

METHOD DETAILS

Protein expression and purification

Various proteins were generated using standard PCR-based methods, cloned into vectors containing an N-terminal Trx-His_6/ His_6-affinity tag followed by an HRV 3C cutting site. All mutants were confirmed by DNA sequencing. Recombinant proteins were expressed in *Escherichia coli* BL21 cells in LB medium at 16°C overnight and protein expression was induced by 0.25 mM IPTG (final concentration) at OD_{600} between 0.6-0.8. Uniformly ^{15}N-labeled PSD-95 NPDZ12 and Stg_CT for NMR analysis was prepared by growing bacteria in M9 minimal medium using $^{15}NH_4Cl$ as the sole nitrogen source. Normally, recombinant proteins were freshly purified using a nickel-NTA agarose affinity column followed by a size-exclusion chromatography (Superdex 200 or Superdex 75) with a column buffer containing 50 mM Tris, pH 8.0, 100 mM NaCl, 1 mM EDTA, 2 mM DTT.

For MAGUK full-length proteins (reference sequences, PSD-95: UniProt, P78352-1; SAP102: NCBI, NP_113827), after the initial step of size-exclusion chromatography by Superdex 200, a mono Q column was applied to remove DNA contamination and degraded proteins. After cleavage by HRV 3C protease, Trx tag was further separated by another step of size-exclusion chromatography using Superdex 200 containing 50 mM Tris, pH 8.0, 100 mM NaCl, 1 mM EDTA, 2 mM DTT.

For TARP_CT (reference sequences, Stg: NCBI, NP_031609; TARP γ-8: NCBI, NP_573453, without Ala341-Ala349 in our template), to fully remove degraded products from the intact TARP_CT, two sequential size-exclusion chromatography using Superdex 75 with a column buffer containing 50 mM Tris, pH 8.0, 300 mM NaCl, 1 mM EDTA, 2 mM DTT were used. After affinity tag cleavage by HRV 3C protease, a mono S column was used to remove the Trx tag and DNA contamination from TARP_CT. Proteins were finally purified and exchanged into buffer containing 50 mM Tris, pH 8.0, 100 mM NaCl, 1 mM EDTA, 2 mM DTT by Superdex 75.

Protein fluorescence labeling

For amide labeling: Highly purified proteins were exchanged into a $NaHCO_3$ buffer (containing 100 mM $NaHCO_3$ pH 8.3, 100 mM NaCl, 1 mM EDTA and 2 mM DTT) and concentrated to 5-10 mg/mL. Alexa 488 NHS ester (ThermoFisher), Alexa 647 NHS ester (Invitrogen) and Cy3/iFluor 405 NHS ester (AAT Bioquest), were dissolved by DMSO and incubated with the corresponding protein at room temperature for 1 hour (fluorophore to protein molar ratio was 1:1). Reaction was quenched by 200 mM Tris, pH 8.2.

For Cysteine labeling

Cysteine-containing His6 Stg proteins (WT and mutants) were prepared in labeling buffer (50mM Tris pH 7.5, 100mM NaCl, 1mM EDTA and 1mM TCEP) with final concentration of 2 mg/mL. iFluor 555 maleimide (10 mg/mL in DMSO) were added with 1:1 protein-to-fluorophore molar ratio and incubated for 1 hour at room temperature.

The fluorophores and other small molecules were removed from the proteins by passing the reaction mixture through a Hitrap desalting column with buffer containing 50 mM Tris, pH 8.0, 100 mM NaCl, 1 mM EDTA, and 2 mM DTT. Fluorescence labeling efficiency was measured by Nanodrop 2000 (ThermoFisher). In imaging assays, fluorescence labeled proteins were further diluted with the corresponding unlabeled proteins in the same buffer. Dilution ratio was illustrated in each figure legend.

Phase transition sedimentation and imaging assay

Proteins were prepared in buffer containing 50 mM Tris, pH 8.0, 100 mM NaCl, 1 mM EDTA, and 2 mM DTT (with affinity tags cleaved and removed) and pre-cleared via high-speed centrifugations. Proteins were then mixed or diluted with buffer to designed combinations and concentrations.

For sedimentation assay, typically, the final volume of each reaction is 100 μl. After 10 min equilibrium at room temperature, protein samples were subjected to sedimentation at 16,873*g* for 10 min at 22°C on a table-top temperature-controlled micro-centrifuge. After centrifugation, the supernatant and pellet were immediately separated into two tubes. The pellet fraction was thoroughly re-suspended with the same buffer to the equal volume as supernatant fraction. Proteins from both fractions were analyzed by 12.5% SDS-PAGE with Coomassie blue staining. Band intensities were quantified using the ImageJ software.

For imaging assay, protein samples were injected into a homemade flow chamber (comprised of a glass slide sandwiched by a coverslip with one layer of double-sided tape as a spacer) for DIC and fluorescent imaging (Nikon Ni-U upright fluorescence microscope) at room temperature. Glasses were washed by Hellmanex II (Hëlma Analytics) and 2 M NaOH sequentially and thoroughly rinsed with MilliQ H_2O before chamber making. During imaging, the chamber was sealed by nail polish to reduce solution evaporation. Image fluorescence intensities were analyzed by the ImageJ software.

Fluorescence recovery after photobleaching assay

FRAP assay was performed on a Zeiss LSM 880 confocal microscope at 20-23°C. The fluorescence intensity difference between pre-bleaching and at time 0 (the time point right after photobleaching pulse) was normalized to 100%. The experimental control is to quantify fluorescence intensities of similar droplet or membrane region without photobleaching. All data were collected within 90 min after LLPS formation.

Isothermal titration calorimetry assay

ITC measurements were carried out on a Microcal VP-ITC calorimeter at 25°C. Proteins used for ITC measurements were dissolved in an assay buffer composed of 50 mM Tris, pH 8.0, 100 mM NaCl, 1 mM EDTA, and 2 mM DTT. Affinity tags on most proteins were cleaved and removed. Except for Stg_PBM, proteins with and without a N-terminal Trx tag were compared and showed no difference in PSD-95 binding. High concentration of protein was loaded into the syringe and titrated into the cell containing low concentration of corresponding interactors (concentrations for each reaction are indicated in the figure legends). For each titration point, a 10 μL aliquot of a protein sample in the syringe was injected into the interacting protein in the cell at a time interval of 2 min. Titration data were analyzed using the Origin7.0 software and fitted with the one-site binding model.

Lipid bilayer preparation and phase transition assay

Small unilamellar vesicle (SUV) preparation, chambered cover glass wash and lipid coating, lipid bilayer phase transition assay are similar as previously described (Zeng et al., 2018) except that 2%–10% PIP2 (Echelon Biosciences) were introduced as indicated in the figure.

NMR spectroscopy

NMR samples contained 0.1 mM of the uniformly ^{15}N-labeled PSD-95 NPDZ12 or Stg_CT were initially prepared in 50 mM Tris, 100 mM NaCl, 1 mM DTT and 1 mM EDTA at pH 7.0. NMR spectra were acquired at 25°C on Varian Inova 750- or 800-MHz spectrometers each equipped with an actively z-gradient shielded triple resonance probe. pH or temperature adjustment were indicated in the figure legend. The backbone assignments of PSD-95 PDZ12 was obtained using the data from our previous study (Wang et al., 2009). The chemical shift difference of each peak shown in Figure 3D is defined as $\Delta p.p.m. = [(\Delta\delta HN)^2 + (\alpha N^*\Delta\delta HN)^2]^{1/2}$. The scaling factor ($\alpha N$) used to normalize the ^1H and ^{15}N chemical shift is 0.17. The peak intensity data shown in Figure 3F were derived by comparing of ^1H,^{15}N HSQC peak intensities of apo NPDZ12 with the corresponding residue of NPDZ12 in the presence of three molar ratios of various Stg_CT mutants. Intensity ratio was defined as NPDZ12 complex peak intensity/apo NPDZ12 peak intensity.

Stg_CT_Δ4 mutants were each titrated into ^{15}N-labeled NPDZ12 (0.1 mM) with the final titration point at the three molar ratio amount of Stg_CT_Δ4 mutants to NPDZ12.

Mouse genetics

Animals were housed according to the University of California, San Francisco (UCSF)'s Institutional Animal Care and Use Committee (IACUC) guidelines. *Gria1–3$^{fl/fl}$* mice were genotyped as previously described (Lu et al., 2009). All experimental protocols involving animals were reviewed and approved by the UCSF's IACUC.

Electrophysiology

Slice cultures were prepared from P6–P8 *Gria1–3$^{fl/fl}$* mouse pups as described previously (Stoppini et al., 1991) and biolistically transfected (Helios Gene Gun (Biorad)) at 1 DIV. Whole-cell voltage-clamp recordings were performed as described previously (Lu et al., 2009). Simultaneous dual recordings were taken from GFP positive (transfected), as identified by nuclear (Cre-GFP) and cytoplasmic (GluA1-TARP γ-8-IRES-GFP) epifluorescence, and neighboring control CA1 pyramidal neurons at 22-24 DIV in organotypic slice cultures. For recording, slices were placed in a perfusion chamber on an Olympus BX51WI upright microscope and perfused at 2.5 ml/min with artificial cerebrospinal fluid (aCSF) containing (in mM): 119 NaCl, 2.5 KCl, 1 NaH_2PO_4, 26.2 $NaHCO_3$ and 11 glucose, 4 $CaCl_2$, 4 $MgSO_4$, 0.1 picrotoxin, 0.02 bicuculline and 2 μM 2-chloroadenosine. The aCSF was bubbled with 95% O_2 and 5% CO_2, and osmolarity was adjusted to 302-305 mOsm. The internal whole-cell recording solution contained (in mM) 135 $CsMeSO_4$, 8 NaCl, 10 HEPES, 0.3 EGTA, 5 QX-314, 4 Mg-ATP, and 0.3 Na-GTP and 0.1 spermine. Osmolarity was adjusted to 290-292 mOsm, and pH at 7.3–7.4. Synaptic responses were evoked by stimulating with a bipolar stimulation electrode (Microprobes) placed in the *stratum radiatum*, and responses were evoked at 0.2 Hz. Surface currents were evoked with Glu (1mM) using a Picospritzer II (General Valve) at 0.1 Hz.

To ensure stable recording, membrane holding current, input resistance, and pipette series resistance were monitored throughout the experiment. Data were gathered through a MultiClamp 700B amplifier (Axon Instruments), filtered at 2 kHz, and digitized at 10 kHz. AMPAR-mediated responses were isolated by voltage-clamping the cell at −70 mV, whereas NMDARs were recorded at +40 mV, with amplitudes taken 150 ms after stimulation to avoid contamination by AMPAR current. To examine AMPAR EPSC synaptic rectification, 0.1 mM D(-)-2-amino-5-phosphonovaleric acid (AP5) was washed in to block NMDAR. Rectification was calculated as follows: RI = 7(I40 – I0)/4(I0 – I70) where Ix represent EPSC amplitude at x mV.

In vivo AMPAR replacement

For AMPAR replacement experiments *in vivo*, *Gria1-3$^{fl/fl}$* mouse brains were transfected in utero with pFUGW-Cre:GFP and pCAGGS-GluA1-TARP_γ-8_R8A constructs at E15.5.

In utero electroporation was performed as follows: E15.5 pregnant Gria1-3$^{fl/fl}$ mice were anesthetized with 2% isoflurane in O_2. For analgesia, 0.05 mg/kg buprenorphine (Reckitt Benckiser Healthcare) and 0.2 mg/kg meloxicam (Boehringer Ingelheim) were injected subcutaneously after induction of anesthesia. Embryos were then exposed out of the abdominal cavity and 1.5 μl of mixed plasmid DNA were injected into the lateral ventricle using a beveled glass micropipette. pFUGW-Cre:GFP (0.5 μg/μl final concentration) was mixed with pCAGGS-GluA1-TARP_γ-8_R8A (1.5 μg/μl final concentration). 0.1% Fast Green (Sigma Aldrich) was added to the DNA mix to help visualization of the injection site. After injection, embryos were electroporated with 5 pulses of 40 V during 50 msec, delivered at 1 Hz, using platinum tweezertrodes (BTX Harvard Apparatus) with a square-wave pulse generator (BTX Harvard Apparatus). To maximize electroporation of the hippocampus, the positive electrode was placed in the lower right hemisphere and the negative electrode placed in the upper left hemisphere. After electroporation, the embryos were placed into the abdominal cavity and the abdominal muscle and skin were sutured. Pregnant females were maintained on a heated pad and monitored during the surgical procedure and the post-surgery period.

Acute slice electrophysiology and LTP induction

300 μm transverse acute slices were cut from P20-26 electroporated mice using a Microslicer DTK-Zero1 (Ted Pella) in chilled high sucrose cutting solution containing (in mM): 2.5 KCl, 7 $MgSO_4$, 1.25 NaH_2PO_4, 25 $NaHCO_3$, 7 glucose, 210 sucrose, 1.3 ascorbic acid. The slices were then incubated for 30 min at 34°C in aCSF containing (in mM): 119 NaCl, 2.5 KCl, 1 NaH_2PO_4, 26.2 $NaHCO_3$, 11 glucose, 2.5 $CaCl_2$ and 1.3 $MgSO_4$. The slices were then transferred to the recording chamber and 0.1 mM picrotoxin and 0.02 mM bicuculline were added to the aCSF for recordings. Simultaneous dual recordings were taken from GFP positive (transfected), as identified by nuclear (Cre-GFP) and cytoplasmic (GluA1-TARP γ-8-IRES-GFP) epifluorescence, and neighboring control CA1 pyramidal neurons. LTP was induced by stimulating Schaffer collateral axons at 2 Hz for 90 s while clamping the cell at 0 mV, after recording a ~3 min baseline, but not more than 5 min after breaking into the cell. Synaptic responses before (baseline) and after LTP induction were evoked at 0.1 Hz. In some cases, one of the two cells was lost at some point during the LTP experiment. Recordings were considered until that point, which result in larger SEM in later stages of the LTP experiment. In cases where only one cell was lost, the remaining cell was considered for the averages. Unpaired statistics were used as a result to determine statistical significance of the LTP experiment.

QUANTIFICATION AND STATISTIC ANALYSIS

For biochemical analysis of bindings, typically three or more independent batches of experiments were used to derive final data, and results are represent as mean ± SD. For FRAP analysis of liquid droplets/clusters, averaged signals from 10 or more droplets/clusters with similar sizes were averaged and plotted as mean ± SD. For electrophysiology, sample sizes (8-19) were chosen on the basis of similar experiments in the field and Power Analysis with preliminary results. Data are represented as mean ± SEM.

For NMR peak intensity analysis reported in Figure 3F, statistical significance was analyzed using one way ANOVA with Bonferroni multiple comparison test. ****, $p < 0.0001$; ns, not significant.

Statistical significance was analyzed using the Wilcoxon signed-rank test in Figures 6F–6J and Mann–Whitney U test in Figure 6L. One way ANOVA with Bonferroni multiple comparison test was used to compare relevant groups in Figure 6K. * $p < 0.05$, ** $p < 0.01$.* $p < 0.05$, ** $p < 0.01$, and *** $p < 0.001$ versus control condition. # $p < 0.05$ versus GluA1-γ-8_Δ4 condition. Statistical significance was analyzed using the Wilcoxon signed-rank test for data in Figure 7C. Mann–Whitney U test was used in Figure 7D. * $p < 0.05$, ** $p < 0.01$.

DATA AND CODE AVAILABILITY

The published article includes all data generated or analyzed during this study.